A 3-D VASCULAR CONNECTIVITY TRACKING AND VASCULAR NETWORK EXTRACTION TOOLKIT

A THESIS SUBMITTED TO
THE GRADUATE SCHOOL OF NATURAL AND APPLIED SCIENCES
OF
MIDDLE EAST TECHNICAL UNIVERSITY

BY

KERİM KARA

IN PARTIAL FULFILLMENT FOR THE REQUIREMENTS
FOR
THE DEGREE OF MASTER OF SCIENCE
IN
BIOMEDICAL ENGINEERING

APRIL 2011

Approval of the thesis:

A 3-D VASCULAR CONNECTIVITY TRACKING AND VASCULAR NETWORK EXTRACTION TOOLKIT

submitted by **KERİM KARA** in partial fulfillment of the requirements for the degree of **Master of Science in Biomedical Engineering Department, Middle East Technical University** by,

Prof. Dr. Canan Özgen
Dean, Graduate School of **Natural and Applied Sciences** __________

Prof. Dr. Semra Kocabıyık
Head of Department, **Biomedical Engineering** __________

Prof. Dr. B. Murat Eyüboğlu
Supervisor, **Electrical and Electronics Engineering Dept., METU** __________

Prof. Dr. H. Saruhan Çekirge
Co-supervisor, **Dept. of Radiology, Hacettepe University** __________

Examining Committee Members:

Prof. Dr. Nevzat G. Gençer
Electrical and Electronics Engineering Dept., METU __________

Prof. Dr. B. Murat Eyüboğlu
Electrical and Electronics Engineering Dept., METU __________

Prof. Dr. Gerhard Wilhelm Weber
Institute of Applied Mathematics, METU __________

Assist. Prof. Dr. Yeşim Serinağaoğlu Doğrusöz
Electrical and Electronics Engineering Dept., METU __________

Assoc. Prof. Dr. Serdar Geyik
Dept. of Radiology, Hacettepe University __________

Date: 25.04.2011

I hereby declare that all information in this document has been obtained and presented in accordance with academic rules and ethical conduct. I also declare that, as required by these rules and conduct, I have fully cited and referenced all material and results that are not original to this work.

Name, Last Name: Kerim Kara

Signature:

ABSTRACT

A 3-D VASCULAR CONNECTIVITY TRACKING AND VASCULAR NETWORK EXTRACTION TOOLKIT

Kara, Kerim

M.Sc., Department of Biomedical Engineering
Supervisor: Prof. Dr. B. Murat Eyüboğlu
Co-supervisor: Prof. Dr. H. Saruhan Çekirge

April 2011, 93 Pages

During angiography procedure, contrast medium is injected into circulatory system of patients and the mostly preferred technique is X-ray angiography. Due to their adverse effects, excess use of contrast medium and X-ray is avoided. For diagnosis, treatment planning, and risk assessment purposes, interventional radiologists utilize visual inspection to determine connectivity relations between vessels. This situation leads angiography to have more adverse effects, since it requires additional injection of contrast medium and X-ray dose.

This thesis work presents a 3-D vascular connectivity tracking toolkit for automated extraction of vascular networks in 3-D medical images. The proposed method automatically extracts the vascular network connected to a user-defined point in a user-defined direction, and requires no further user interaction. The toolkit prevents additional injection of contrast agent and X-ray dose, saves time for the interventional radiologist.

While the algorithm is applicable on all 3-D angiography images, performance of the method is observed on 3-D catheter angiography image of cerebrovascular structures. The algorithm iteratively tracks gravity centers of vascular branches in the user-defined direction, preserving connection to the user-defined point. Curvy branches are tracked even if they have discontinuous portions. Since this tracking method does not depend on lumen diameter and intensity differences, branches with stenoses and branches having large intensity difference can be successfully tracked. Skeletonization and junction detection methods are described, which are used to detect the sub branches, indirectly connected to the point. These methods are capable of handling bifurcations, trifurcations, and junctions having more branches. However, false junctions occurring due to superposition of vessels are not eliminated.

Keywords: Angiography, vascular network, 3-D medical image processing, connectivity, tracking, skeletonization, junction detection

ÖZ

3-B VASKÜLER BAĞLANIRLIK İZLEYİCİSİ VE VASKÜLER AĞ ÇIKARTMA ARAÇ TAKIMI

Kara, Kerim

Yüksek Lisans, Biyomedikal Mühendisliği Bölümü
Tez Yöneticisi: Prof. Dr. B. Murat Eyüboğlu
Ortak Tez Yöneticisi: Prof. Dr. H. Saruhan Çekirge

Nisan 2011, 93 Sayfa

Anjiyografi işleminde çoğunlukla X-ışını yöntemi kullanılmakta ve hastanın dolaşım sistemine kontrast madde verilmektedir . İstenmeyen etkilerinden dolayı fazla X-ışını ve kontrast madde kullanımından kaçınılmalıdır. Teşhis, tedavi planlama ve risk değerlendirme amaçlarıyla girişimsel radyologlar görsel olarak inceleme yapmaktadır. Bu durum, daha fazla kontrast madde ve X-ışını dozu gerektirdiğinden, anjiyografinin istenmeyen etkilerini artırmaktadır.

Bu tez çalışmasında, 3-B tıbbi görüntülerdeki damar ağlarının otomatik olarak çıkartılması için bir 3-B vasküler ağ çıkarma araç takımı sunulmaktadır. Önerilen yöntem, kullanıcı tarafından belirtilen bir noktaya yine kullanıcı tarafından tanımlanan yönde bağlı olan vasküler ağı otomatik olarak çıkarmakta, ilave bir kullanıcı etkileşimi gerektirmemektedir. Böylece, daha fazla kontrast madde enjeksiyonuna ve X-ışını dozuna başvurulmasının önüne geçmekte, girişimsel radyoloğa zaman kazandırmaktadır.

Tüm 3-B anjiyografi görüntülerine uygulanabilen bu algoritmanın performansı, kateter anjiyografi ile elde edilmiş 3-B beyin damar görüntüleri üzerinde gözlenmiştir. Algoritma, kullanıcı tarafından belirtilen noktaya bağlantıyı

koruyarak, vasküler dalların ağırlık merkezlerini tekrarlı bir biçimde kullanıcı tarafından tanımlanan yönde takip etmektedir. Eğri dallar da, kopuk parçalara sahip olsalar bile takip edilebilmektedir. Bu takip yöntemi lumen çapına ve koyuluk farkına bağlı olmadığından dolayı, stenozlu dallar ve yüksek koyuluk farkına sahip dallar da takip edilebilir. İlgili noktaya dolaylı olarak bağlanan alt dalların tespit edilmesi için, iskeletleştirme ve kavşak tespit yöntemleri de açıklanmıştır. Bu yöntemler çatallanımları, trifurkasyonları ve daha fazla dala sahip kavşakları ele alabilmektedir. Ancak, damarların bitişik biçimde üst üste gelmesinden kaynaklanan yanlış kavşaklar ortadan kaldırılamamıştır.

Keywords: Anjiyografi, vasküler ağ, 3-B tıbbi görüntü işleme, bağlanırlık, izleme, iskeletleştirme, kavşak tespiti

On behalf of Dr. Kerim Kara (1965-2010),
to my family ...

ACKNOWLEDGEMENTS

For their supervisions, I owe thanks to Prof. Dr. Murat Eyüboğlu and Prof. Dr. Saruhan Çekirge. Effort is unprizable and they put greatest efforts to achieve this work; made this thesis work possible.

Fortunately METU brought me together with Alper Çevik, I must express my pleasure since we shared years of great partnership and cooperation. On the other hand, I must gratefully mention Ceren Bora, for her unforgettable support on my academic and administrative troubles.

Prof. Dr. Ergin Atalar and Assoc. Prof. Dr. Vakur Ertürk provided a huge amount of activation energy to me by demonstrating how R&D is passionately loved and how we can serve humanity through science. It is that energy still carries me towards; I respectfully and thankfully admit.

It is a great pleasure for me to be a part of Hacettepe University Interventional Neuroradiology team. I am heartily thankful to Prof. Dr. Işıl Saatçi Çekirge, Assoc. Prof. Dr. Kıvılcım Yavuz, and Assoc. Prof. Dr. Serdar Geyik - for their clinical guidance, who made all the efforts meaninful and valuable- and Mevlüt Çoban, Atilla Topaloğlu, Halil Uğurlu, Süleyman Kalaycı, Müjdat Işıklar, and Adem Kütük –for their great hospitality.

I must give thanks to those three wise AX-men; Kadir Afacan, Tolga Çit, Beytul Geredeli for their technical guidance; Dr. Haydar Çelik, Tunca Korkmaz, and Orçun Özbek who have strengthened me to keep going on; and lab-mates Volkan Emre Arpınar, Evren Değirmenci, Rasim Boyacıoğlu, Tankut Topal, Ali

Ersöz, İlhan Soner Keçeli, and Balkar Erdoğan - every minute to be missed. Furthermore, it is an honour for me to have the last rocky roads walked towards graduation together with Ali Reza Mazloumi Gavgani and Ersin Karcı.

I am all aware of their precious efforts, I sincerely thank to Dr. Alper Alsan for his educational and professional coaching; my home-mates Ümit Aydın and Uğur Cünedioğlu for their comprehensive support; Saadeddin Tekin for his life coaching; Asst. Prof. Dr. İlkay Ulusoy for her image processing knowledge sharing; Doydos and Fatih Kaya for their meaningful brotherhood. I deserve nothing more than I get.

Finally, in the names of Ayşe Kavas, Mehmet Kavas, Bünyamin Eker, Beyhan Eker, Esra Özdemir, Burak Özdemir, and Elif Eker, I owe thanks to my great family. Thanks, we are all together.

TABLE OF CONTENTS

ABSTRACT iv

ÖZ vi

ACKNOWLEDGEMENTS ix

TABLE OF CONTENTS xi

LIST OF TABLES xiv

LIST OF FIGURES xv

CHAPTERS

1. INTRODUCTION 1

  1.1. Motivation of the Thesis Work 1

  1.2. Scope of the Thesis Work 4

  1.3. Outline of the Thesis 7

  1.4. Background Information 7

    1.4.1. Cerebrovascular Anatomy 7

    1.4.2. Main Cerebrovascular Diseases 15

    1.4.3. Cerebrovascular Imaging 21

  1.5. Problem Definition 24

2. THEORY 25

  2.1. Literature Review 25

    2.1.1. Vessel Tracking 25

    2.1.2. Skeletonization 29

2.1.3. Junction Detection 32

2.1.4. Region Growing 33

2.2. Methods 35

2.2.1. Tracking Single Vascular Branches 35

2.2.2. Skeletonization 38

2.2.3. Pruning 46

2.2.4. Junction-Detection 46

2.2.5. Volume-Growing 47

2.2.6. Setting New Initiators 50

3. RESULTS AND DISCUSSION 52

3.1. Single Branch Tracking 52

3.2. Skeletonization 60

3.3. Junction Detection 65

3.4. Distinguishing Junctions on the Tracked Branch 68

3.5. Setting New Tracking Initiators 68

4. PERFORMANCE EVALUATION 73

4.1. Evaluation Methods 73

4.1.1. Performance Evaluation on Real Patient Image Data 73

4.1.2. Performance Evaluation on Physical Phantom's Image Data 75

4.2. Evaluation Results 80

4.2.1. Performance of the Algorithm on Real Patient Image Data 80

4.2.2. Performance of the Algorithm on Image Data from the Physical Phantom 82

5. CONCLUSION AND FUTURE WORK 84

5.1. Conclusion 84
5.2. Future Work 87
REFERENCES 88

LIST OF TABLES

TABLES

Table 1-1 - Top ten causes of death, all ages, Turkey, 2002. 2

Table 1-2 - Arterial vascular anatomy of the brain, proximal arteries are handled from arch of aorta till distal branches [**7**]. 11

Table 2-1 - Euler table for preserving Euler characteristic 43

Table 4-1 - Numbers of true positives, false positives, true negatives, and false negatives in patient data as counted by the radiologists.................................. 80

Table 4-2 - Calculated values of sensitivity, specificity, false negative rate, and false positive rate corresponding to patient data... 81

Table 4-3 - Numbers of true positives, false positives, true negatives, and false negatives in the synthetic object, while the object has no superposing branches 82

Table 4-4 - Calculated values of sensitivity, specificity, false negative rate, and false positive rate corresponding to the synthetic object with no superposing branches 82

Table 4-5 - Numbers of true positives, false positives, true negatives, and false negatives in the synthetic object, while the object has two superposing branches 83

Table 4-6 - - Calculated values of sensitivity, specificity, false negative rate, and false positive rate corresponding to the synthetic object with two superposing branches 83

LIST OF FIGURES

FIGURES

Figure 1.1- Anterior circulation and posterior circulation with their main connections [5]. 8
Figure 1.2 - The Circle of Willis [8]. 9
Figure 1.3 - Lateral view of two main variations of the anterior cerebral artery; a)secondary branches originate from the callosomarginal artery, a main branch of the anterior cerebral artery; b) secondary branches arise directly from the anterior cerebral artery [6]. 12
Figure 1.4 - Lateral view of two variants of the middle cerebral artery; a) with a bifurcation A,B; b) with a trifurcation A,B,C [6]. 13
Figure 1.5 - Lateral view of the infratentorial artery with its connection to internal carotid artery [6]. 14
Figure 1.6 - Lateral view of the posterior cerebral artery [6]. 15
Figure 1.7 - 2-D angiographic image of cerebral vessels, where the arrow points at an occlusion [9]. 16
Figure 1.8 - A graphical illustration of a saccular brain aneurysm. To prevent rupture of aneurysms, a coil is placed into it so that blood supply into the aneurysm is blocked [10]. 18
Figure 1.9 - A real 3-D image of cerebral vessels, where the arrow points at a saccular aneurysm [11]. 19
Figure 1.10 - The AVM is seen as a dense collection of vessels (the nidus) that connect the arteries directly to the veins without an intervening capillary system [12]. 20

Figure 1.11 - After Treatment: the AVM is cleared, allowing better circulation [12]. ... 21
Figure 1.12 - Angiography setup [5]. ... 23
Figure 2.1 - Single vascular branch tracking iteration. The iteration is terminated when intensity of voxels go under a specified value ... 35
Figure 2.2 - Local box around a point $\boldsymbol{Pi}$ in the direction $\boldsymbol{Di}$. $\boldsymbol{Di}$ stays in the center of the box' base. The dimension of base is $\boldsymbol{li} \times \boldsymbol{mi}$, while $\boldsymbol{Hi}$ is the height of box ... 36
Figure 2.3 - Illustration of voxels which are *n*-adjacent to $\boldsymbol{p}$. a) *n* = 6, b) *n*=18, c) *n*=26 ... 38
Figure 2.4 - Special neighbors of $\boldsymbol{p}$. These voxels are used to determine what type of a border point $\boldsymbol{p}$ is. If *N*=0, $\boldsymbol{p}$ is a border point of type-N. If *S*=0, $\boldsymbol{p}$ is a border point of type-S. If *E*=0, $\boldsymbol{p}$ is a border point of type-E. If *W*=0, $\boldsymbol{p}$ is a border point of type-W. If *U*=0, $\boldsymbol{p}$ is a border point of type-U. If *D*=0, $\boldsymbol{p}$ is a border point of type-D. ... 40
Figure 2.5 - a) A 2 × 2 × 2 octant, $\boldsymbol{N2}(\boldsymbol{v})$; b) An example octant with a configuration corresponding to binary 11111011. Note that black points have value 1, and white points have value 0. ... 41
Figure 2.6 - Iterative procedure and decision-tree of skeletonization algorithm. 45
Figure 2.7 - Preprocessing phase, in which 3-D vessel images are prepared for skeletonization. ... 46
Figure 2.8 - Region growing process in the lowest slice of a local box. ... 48
Figure 2.9 - Region growing process in the higher slices of a local box. ... 49
Figure 2.10 - Illustration of the entire volume growing process. ... 50
Figure 2.11 - Illustration on setting the new initiators. a) A cubic volume is created around the distinguished junction. b) Branches, 26-connected to the junction, are determined. c) Foreign branches are removed. d) Intersections of branches' skeleton with the cube surfaces are searched. e) Vectors through the junction and the intersection points are calculated. f) Previously tracked

intersections are ignored. The remaining vectors are set to be the next starting directions, where the next starting point is set as the junction. 51

Figure 3.1 - Effect of box dimensions on tracking performance. a) Volume of interest. b) Tracking fails when box dimensions are twice larger than vessel lumen width. The blue rectangle represents the box located at the user-defined starting point in the user-defined starting direction. c) Box dimensions enough to cover the lumen achieves tracking the right track. The blue rectangle represents the box located at the user-defined starting point in the user-defined starting direction. 53

Figure 3.2 - Longer boxes can track the branches with disconnected portions. a) A branch with disconnected branches. b) Tracking procedure could cover it. .. 54

Figure 3.3 - kd affects algorithm's ability to track curvatures. a) A curvy branch. b) k_d = 0 cannot proceed further through a curve. 55

Figure 3.4 - Any nonzero k_d achieves good performance to track curvatures. a) k_d = 10. b) k_d = 100. c) k_d = 3000 (continued). 57

Figure 3.5 - k_p affects the tracking procedure's speed and deliberateness. a) k_p = 0. b) k_p = 3. c) k_p = 5. d) k_p = 7. 58

Figure 3.6 - The limit on the summation of voxels' intensities in a local box affect the capability to cover distal branches. a) An image containing distal branches. b) Limit is set to 10000, distal portion of the branch is not tracked. c) Limit is set to 5000, distal portion of the branch is tracked.. 59

Figure 3.7 - a) Proximal vessels. b) Their skeleton. 61

Figure 3.8 - a) Distal vessels. b) Their skeleton. 62

Figure 3.9 - a) The volume of interest. b) Skeleton of the vessels in the volume. c) Skeleton after pruning operation. d) Voxels, which are removed during pruning (Continued). 64

Figure 3.10 - a) Red dots mark the junctions before pruning operation. b) Red dots mark the junctions after pruning operation. Pruning operation reduced the number of junctions from 244 to 76.. 66

Figure 3.11 - a) Two superposed branches, yielding a false junction. b) The superposed branches are discriminated by a local thresholding procedure, the false junction is removed. 67
Figure 3.12 - A closer look at detected junctions. a) Red dots showing the junctions. One of the junctions pointed by the arrow is due to a skeleton twig. b) Junctions marked by red dots are due to superpositioning of branches. 67
Figure 3.13 - A vascular network, in which the red branch is tracked. 69
Figure 3.14 - Pruned skeleton of the volume of interest.................................. 69
Figure 3.15 - All junctions within the volume of interest. 70
Figure 3.16 - The points Pi of the tracked branch. 70
Figure 3.17 - The recovered branch, recovery is achieved by volume growing around the seed points Pi. 71
Figure 3.18 - Distinguished junctions, located in the grown volume................. 71
Figure 3.19 - The new starting points (big red dots) and corresponding directions (small red dots) Note that superposed neighboring branches are also to be tracked. 72
Figure 4.1 - A sample patient image depicting the starting point and direction as defined by an expert interventional radiologist 74
Figure 4.2 - Physical phantom object, having two branches each with two junctions... 75
Figure 4.3 - 2-D Fluoroscopy image of the physical phantom 77
Figure 4.4 - 2-D projection image of the physical phantom's 3-D angiographic image, created via Matlab. This projection image is used as an interface to set initiators. The artifacts in the images are suppressed by simple global thresholding. 78
Figure 4.5 - Visualization of the physical phantom's 3-D image in Matlab. Since this 3-D image of the physical phantom includes a huge amount of data in it, entire image cannot be visualized in Matlab. 79

CHAPTER 1

INTRODUCTION

1.1. Motivation of the Thesis Work

2004 report of World Health Organization on causes of death includes statistical information on death causes and rates of individual countries for the year 2002[**1**]. According to the report, cardiovascular diseases are a thundering threat for the entire world population: Cardiovascular diseases caused 28% of all deaths in 2002. With a closer look, ischaemic heart diseases caused 12%, cerebrovascular diseases caused 8%, and hypertensive heart diseases caused 2% of all deaths.

Together with the report on causes of death, Mortality Country Fact Sheet 2006 [**2**], which is also published by World Health Organization, exhibits the dramatic effect of cardiovascular diseases on death rates in Turkey. According to the fact sheet, diseases originating from circulatory system are the most common causes of death in Turkey. The report yields that 54% of deaths are caused by cardiovascular diseases: Ischaemic heart diseases caused 24% and cerebrovascular diseases caused 14%, while hypertensive heart diseases caused 3% of total deaths in the year 2002 (Table 1-1).

Table 1-1 - Top ten causes of death, all ages, Turkey, 2002.

Causes	Deaths (000)	Deaths (%)	Years of Life Lost (%)
All causes	436	100	100
Ischaemic heart disease	102	24	14
Cerebrovascular disease	62	14	10
Perinatal conditions	19	5	11
Chronic obstructive pulmonary disease	18	4	2
Lower respiratory infections	12	3	6
Hypertensive heart disease	11	3	2
Trachea, bronchus, lung cancers	10	2	2
Meningitis	7	2	4
Diarrhoeal diseases	6	2	4
Congenital anomalies	6	2	4

Source: Death and DALY estimates by cause, 2002
http://www.who.int/entity/healthinfo/statistics/bodgbddeathdalyestimates.xls

Weights of vascular diseases among the rates of death causes reveal the importance of supporting related clinicians in the decision-making phase. Tools and applications, which can support clinicians in terms of better detecting the problems, offering efficient clinical solutions, speeding the processes up are appreciated. Engineers are expected to put both hardware and software products into clinical service.

While there are different specific groups of clinicians working on cardiovascular diseases, interventional radiologists, who are a special group of radiologists, focus on vascular diseases from the perspective of visualizing the vascular structures and evaluating image data. They utilize special forms of radiation to obtain image data of vessels. Interventional radiologists' decision-making phase covers acquiring and analyzing the image data, accurately diagnosing the pathology, determining risks, and treatment-planning.

Angiography suites are special environments, where are not only used for imaging purposes but also used for diagnosis and treatment operations. Interventional procedures like endovascular neurosurgery operations take place in these suites. While computed tomography (CT) and magnetic resonance (MR) scanners can be used to acquire images and diagnose pathologies, specialized x-ray systems are utilized in angiography suites since they are suitable for vascular treatment purposes as well as image acquisition and diagnosis purposes.

X-ray based angiography (AX) scanners have large flat-panel x-ray detectors, yielding two-dimensional (2-D) projection images at any time instant. A half-circle rotation of x-ray source and detector pair can acquire three-dimensional (3-D) images of large volumes such as entire head and neck or entire abdomen. By utilizing AX scanners together with digital subtraction angiography method, interventional radiologists can obtain 2-D and 3-D images of region-of-interest and volume-of-interest, respectively. Detailed information regarding digital subtraction angiography is provided in the following chapter.

In an angiography suite, patients are generally anaesthetized and interventional radiologists have limited time to complete diagnosis and treatment procedures. Furthermore, digital subtraction angiography procedures require contrast agent injection into circulatory system and the same procedures are implemented under x-ray, especially for treatment purposes. The crucial point here is that both contrast agent and x-ray are invasive. Then, tools, which achieves the process with lower dose and less contrast agent in less time is highly appreciable in an angiography suite.

Tools, which save dose, contrast agent, and time are appreciated by interventional radiologists as long as the tools support the clinicians in terms of diagnosis, risk assessment, and treatment-planning. Appreciable tools are supposed to lead more accurate and faster diagnosis, highlight the risks, and assist in the treatment-planning phase. 2-D and 3-D road-mapping, image registration, image fusion, automated volume calculation, automated pathology detection, dual-volume reconstruction are some examples of such tools.

1.2. Scope of the Thesis Work

Automatically relating the connections between vessels and determining the junctions within a vessel network would provide contrast agent, dose, and time saving opportunities to interventional radiologist. Such a tool, by utilizing 3-D digital subtracted angiography data, could process on connectivity, bifurcation, position of a point / volume of interest, positioning connected components with respect to it, hence, could support clinicians in terms of diagnosis, risk assessment, and treatment-planning.

Automatic detection of vessels, which feed a specified volume, or detecting the network and volume, where a specified vessel feeds would support clinicians during diagnosis procedures. By making use of the same image processing techniques, the tool could support during risk assessment by virtually visualizing the vessel network, which might be occluded during operation. While treatment-planning, it could highlight the path to a specified point in distal, yield the path between two specific points, highlight the vessel network originating from and connected to a specific point. It is apparently conceivable that this tool could support interventional radiologists to consume less contrast agent, dose, and time in angiography suites.

Within this thesis work, we proposed a 3-D vessel connectivity tracking method and a tool. The method is capable of tracking a single branch, detecting junctions, determining bifurcations, trifurcations, etc. on the branches of interest, and automatically starting single-branch tracking procedures. Keeping in mind that the method is applicable to any 3-D digital subtracted angiography data of any organ in the body, which can be obtained via any modality, we have focused on 3-D cerebral vessel data obtained via AX scanners. The 3-D images of cerebral vessels used in the comprehension of this work are acquired by a rotation of AX scanner's C-arm. Hence, "3-D image" within this text also refers to "rotational image", as used by interventional radiologists.

A request by Prof. Saruhan Çekirge from Hacettepe University Faculty of Medicine, has initiated this study. Clinical interests and requirements of Prof. Çekirge and the technical substructure and patient potential at Hacettepe University Faculty of Medicine played determinant role on the scope of this work. As an interventional radiologist focusing on cerebrovascular diseases, Prof. Çekirge led the development and applications of the work to cerebrovascular diseases. Detailed information on the most common cerebrovascular diseases and possible applications of 3-D vessel connectivity tracking on them are given in the following chapter.

This thesis work aims at creating a basic and working platform as a first step to a clinically applicable product in order to promote to human life quality. As a first step, the necessary image processing algorithms and components are generated, implemented, simulated, integrated together, and demonstrated that 3-D vessel connectivity tracking algorithm is achieved. On the other hand, a graphical user interface is provided, so the clinicians can define inputs and observe the outputs.

Although advanced applications of different image processing algorithms, such as central line extraction, region growing, and thresholding are generated and implemented within the context of this thesis work, we have focused on providing an overall working and integrated solution on 3-D vessel connectivity tracking rather than going into details and further improving the mentioned individual algorithms. Therefore, the tool generally achieves 3-D vessel connectivity tracking and it needs further developments in the background components. As a future work, those components would be improved so that the tool could be clinically applicable.

In this study, we propose a branch tracking and a junction detection algorithm; determining vessel network connected to a user-defined point in user-defined direction. Branch tracking algorithm is implementation of the method proposed in [**3**]; iteratively computes gravity center of a local volume, resulting with a single branch tracked. As a single branch connected to a specific seed point is tracked, junction detection algorithm on that branch is executed. A novel 3-D topology preserving centerline extraction method is implemented as an intermediate step to junction detection. This centerline extraction method is a combination of [**3**] and [**4**]. Junctions are detected on the topology preserving centerline, analyzing the junctions on the branch of interest yields new points and directions to start the tracking procedure. Iterative implementation of this method provides the opportunity to discover the vessel network, including the distal vessels, connected to the user-defined point in the user-defined direction. The algorithm has the ability to discover the network even if discontinuities occur on a branch due to image degradations. One disadvantage of the algorithm to note is that it may produce false junctions if super-positioning of vessels are to the subject. A better local thresholding method is necessary to overcome this super-positioning problem and eliminate this disadvantage.

1.3. Outline of the Thesis

As background information on cerebrovascular anatomy, diseases, and imaging techniques, the cerebral vessels and pathologies are necessary to clearly understand the clinical concerns and requirements. The following section covers these topics and constitutes a base for problem definition, which is provided in the last section of this chapter.

Chapter 2 provides a review on related articles in the literature. Also the methods used to achieve the objectives of the entire study are described step by step in this chapter. The methods expressed in Chapter 2 are implemented on cerebral angiographic images; outcoming results are presented and discussed in Chapter 3. Performance evaluation of the entire algorithm is described and the performance results are tabulated in Chapter 4. The overall assessment and conclusion are provided in Chapter 5. Furthermore, a summary on the trend of future work is given in this last chapter.

1.4. Background Information

1.4.1. Cerebrovascular Anatomy

Understanding vascular anatomy of the central nervous system introduces countless benefits not only in clinical terms but also in technical perspectives. Mentioned anatomical understanding provides educated decision-making opportunity for clinicians about evaluation and treatment of patients. On the other hand, anatomical knowledge provides an image-processing engineer to better conceive the possible relations of branches with each other, foresee possible interactions between branches, visual characteristics in different medical imaging techniques, understand clinical requirements, and propose clinically applicable solutions. This section includes a very superficial introductory arterial vascular anatomy of the brain for engineers. Venous anatomy is omitted because it is not observed as a diagnosis and therapy guide for the concerned vascular diseases.

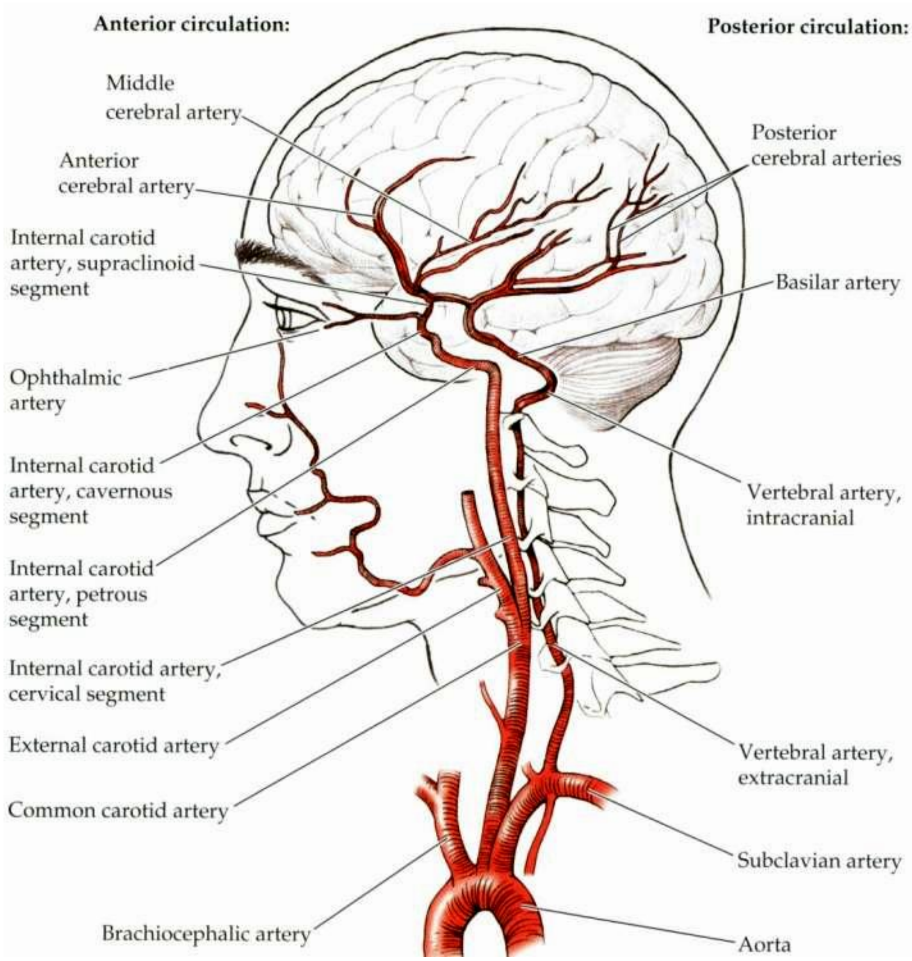

Figure 1.1- Anterior circulation and posterior circulation with their main connections **[**5**]**.

The arterial flow to the cerebral hemispheres is supplied through **anterior circulation** and **posterior circulation** [**5**]. Figure 1.1 shows the anterior and posterior circulations and their main connections.

The **common carotid arteries** originate at the aorta or brachiocephalic arteries, and bifurcate into the **internal carotid arteries** and **external carotid arteries**[**5**]. Bilaterally paired internal carotid arteries run into the carotid canal at the base of skull [**6**] and provide the anterior circulation [**5**,**7**]. The external carotid artery divides in the carotid triangle into branches for organs in the neck, the face, the scalp, and the meninges [**6**,**7**].

Arising from the subclavian arteries, the bilateral **vertebral arteries** proceed to form **basilar arteries** and provide the posterior circulation [**5**]. The brain stem, cerebellum, and the posterior portions of the cerebral hemispheres are supplied by the vertebral and basilar arteries [**7**].

An anastomotic ring **circle of Willis** is the region where the anterior and posterior circulations coincide and from which all the major cerebral vessels arise (Figure 1.2). The circle of Willis provides abundant opportunities for collateral flow; however, a complete ring is present in only approximately 25% of individuals [**5**].

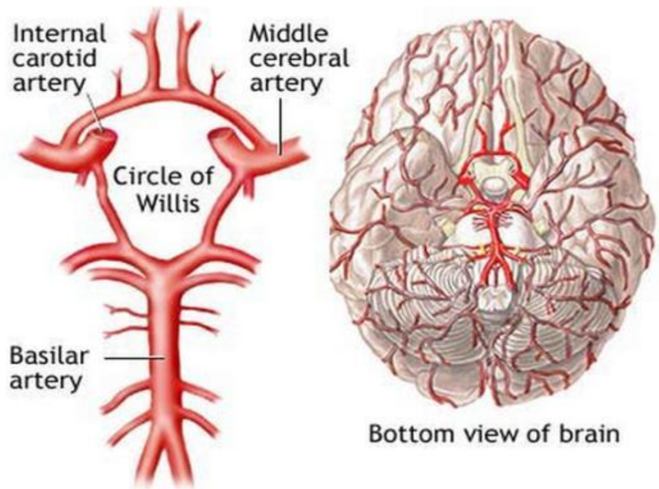

Figure 1.2 - The Circle of Willis **[**8**]**.

The anterior, middle, and posterior cerebral arteries are the main arteries which provide circulation to the cerebral hemispheres. "The **anterior cerebral arteries (ACAs)** (Figure 1.3) and **middle cerebral arteries (MCAs)** (Figure 1.4) are the terminal branches of the internal carotid arteries. The anterior cerebral arteries anastomose anteriorly at the **anterior communicating artery (AComm)**. The anterior and posterior circulations are linked to each other via the **posterior communicating arteries (PComm's)** (Figure 1.5), which connect the internal carotids to the posterior cerebral arteries, thereby joining the anterior and posterior circulations. The **posterior cerebral arteries (PCAs)** (Figure 1.6) arise from the top of the basilar artery, which in turn is formed by the convergence of the two vertebral arteries. In addition to the posterior cerebral arteries, several branches to the brainstem and cerebellum arise from the vertebrobasilar system." [**5**]

The arterial vascular anatomy of the brain is namely summarized in the Table 1-2 [**7**]. Graphical illustrations are provided in figures Figure 1.3, Figure 1.4, Figure 1.5, and Figure 1.6, which help better understanding arterial cerebrovascular anatomy by visualization.

Table 1-2 - Arterial vascular anatomy of the brain, proximal arteries are handled from arch of aorta till distal branches [**7**].

- Arch of the aorta
  - Brachiocephalic (innominate) artery
    - Right common carotid artery
      - Right internal carotid artery
      - Right external carotid artery
    - Right subclavian artery
      - Right vertebral artery
  - Left common carotid artery
    - Left internal carotid artery
    - Left external carotid artery
  - Left subclavian artery
    - Left vertebral artery

- Carotid (anterior) circulation - internal carotid artery
  - Opthalmic artery
  - Anterior choroidal artery
  - Posterior communicating (posterior cerebral artery)
  - Anterior cerebral artery
    - Recurrent artery of Huebner
    - Anterior communicating artery
    - Orbito-frontal artery
    - Fronto-polar artery
    - Calloso-marginal artery
    - Pericallosal artery
  - Middle cerebral artery
    - Lenticulostriate arteries
    - Anterior, middle, and posterior temporal arteries
    - Prefrontal artery
    - Precentral artery
    - Central artery
    - Superior and inferior parietal arteries
    - Angular artery

- Vertebrobasilar (posterior) circulation
  - Vertebral artery
    - Posterior inferior cerebellar artery
    - Anterior spinal artery
  - Basilar artery
    - Anterior inferior cerebellar artery
    - Internal auditory (labyrinthine) artery
    - Penetrating (pontine) arteries
    - Superior cerebellar artery
    - Posterior cerebral artery
      - Interpeduncular-thalamic artery
      - Posterior choroidal artery
      - Thalamo-perforating artery
      - Thalamo-geniculate artery
      - Anterior and posterior temporal arteries
      - Parieto-occpital artery
      - Calcarine artery

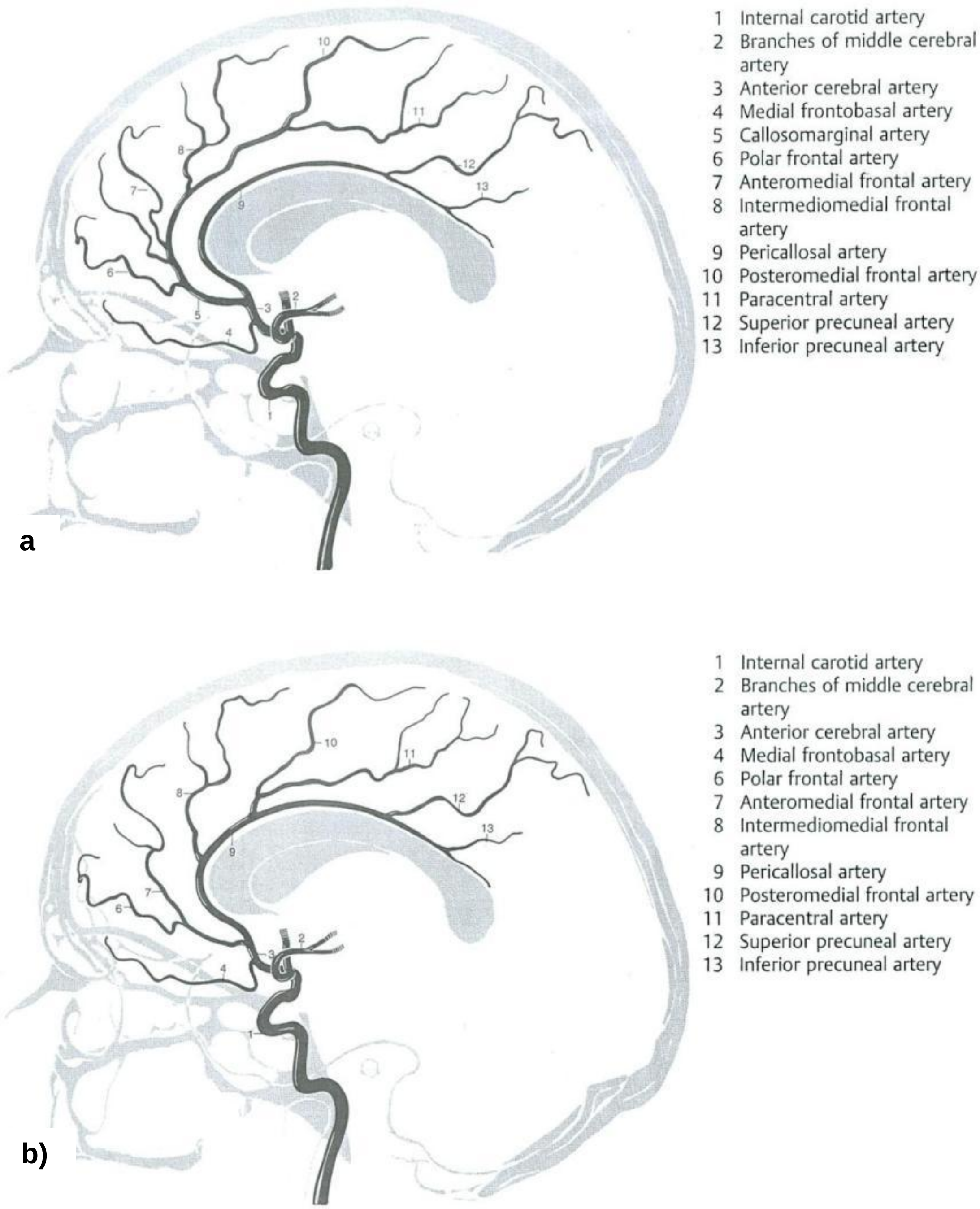

Figure 1.3 - Lateral view of two main variations of the anterior cerebral artery; a)secondary branches originate from the callosomarginal artery, a main branch of the anterior cerebral artery; b) secondary branches arise directly from the anterior cerebral artery **[**6**]**.

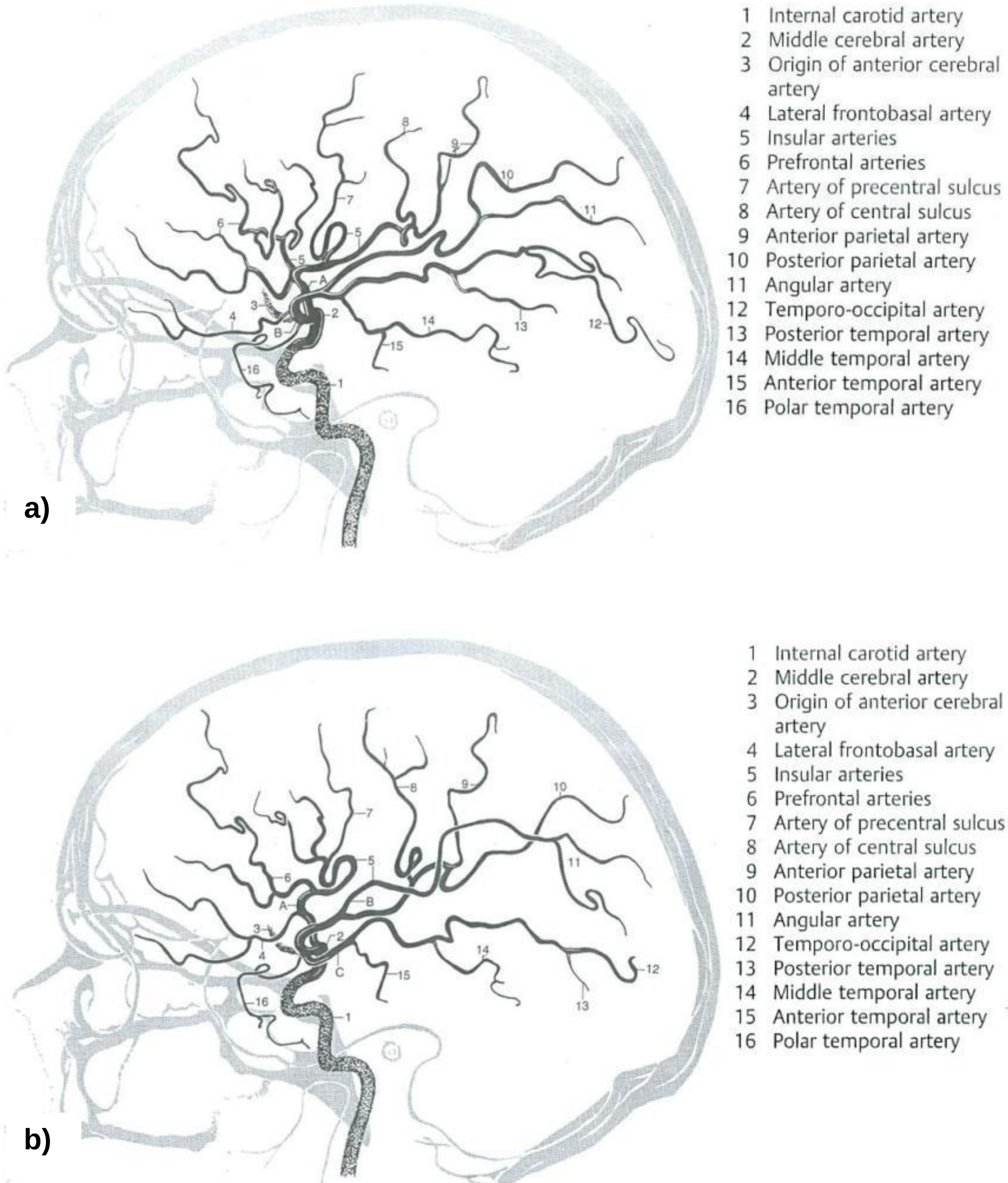

Figure 1.4 - Lateral view of two variants of the middle cerebral artery; a) with a bifurcation A,B; b) with a trifurcation A,B,C **[**6**]**.

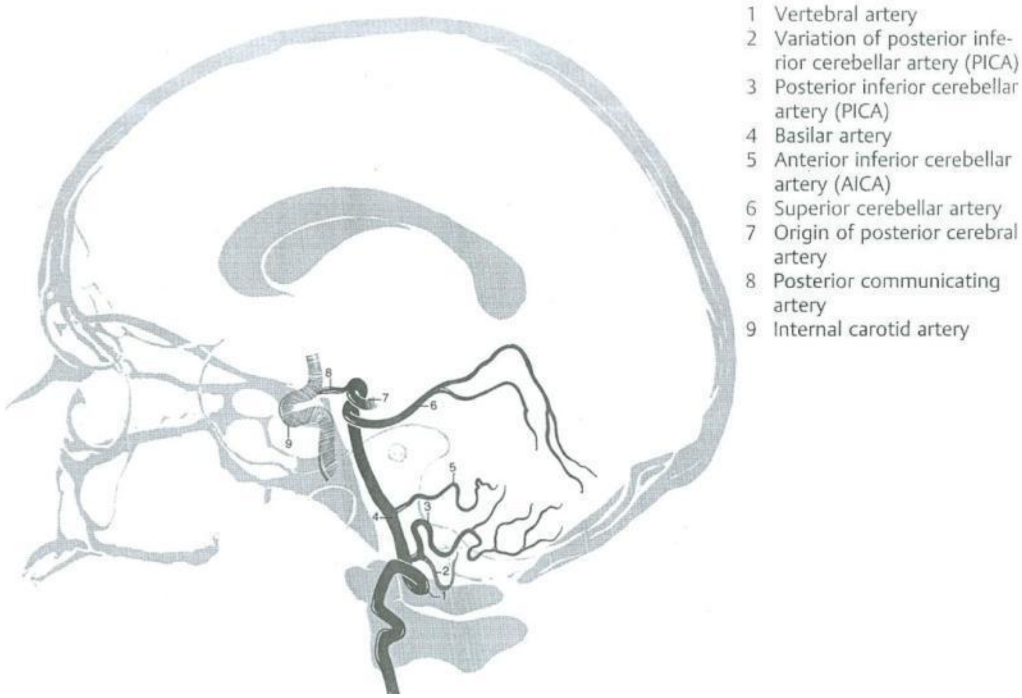

Figure 1.5 - Lateral view of the infratentorial artery with its connection to internal carotid artery **[**6**]**.

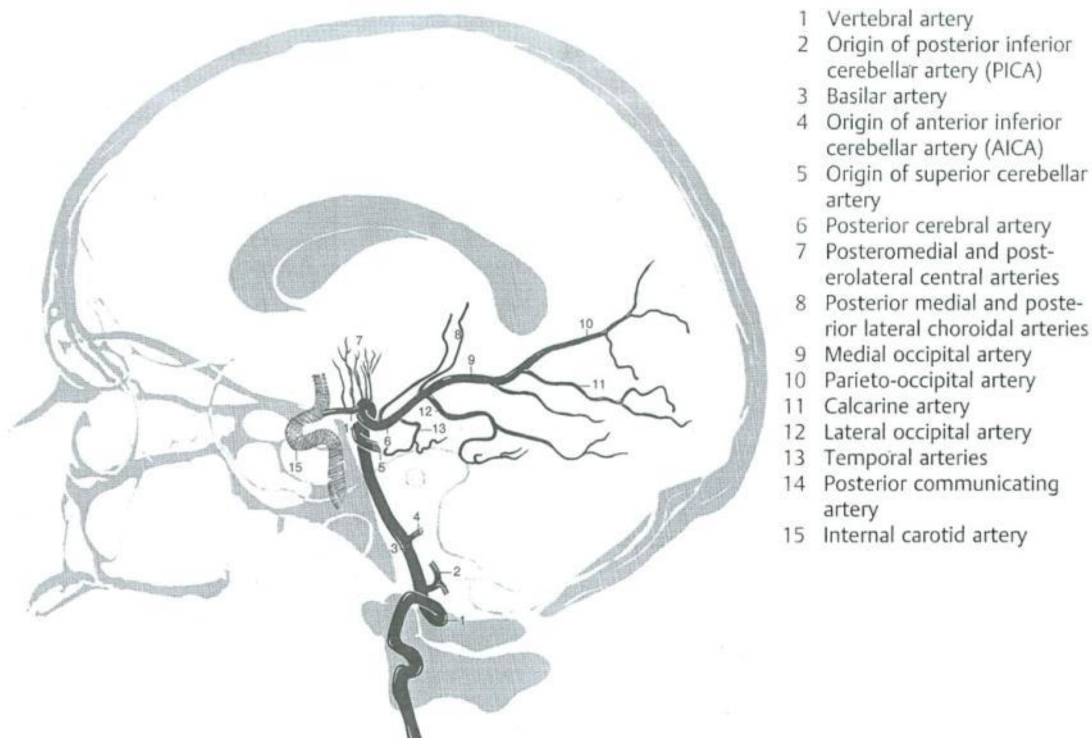

Figure 1.6 - Lateral view of the posterior cerebral artery **[**6**]**.

1.4.2. Main Cerebrovascular Diseases

This section includes an introduction to the most common cerebrovascular pathologies concerned in an angiography suite. Having an overview insight about the causes, results, physics, and mechanisms of these pathologies helps an image-processing engineer to clearly define the problem, understand the clinical requirements and this insight brightens the path leading to a clear solution.

a. Stroke

Most strokes are due to occlusion or rupture of an artery or arteriole. Classifying stroke with respect to its cause, ischemic stroke and hemorrhagic stroke are considered. Figure shows an x-ray image of an occlusion.

Figure 1.7 - 2-D angiographic image of cerebral vessels, where the arrow points at an occlusion **[**9**]**.

Ischemic Stroke

Secondary to arterial occlusion, ischemic stroke causes approximately 80% of all cerebrovascular cases [**7**]. Any mechanism which reduces the amount of blood flowing to the brain and, hence, the central nervous system can result with ischemia [**7**].

Arterial occlusion cases mostly follow thromboembolism [**7**]. "In thrombotic infarcts a blood clot is formed locally on the blood vessel wall, usually at the site of an underlying atherosclerotic plaque, causing the vessel to occlude. In an embolic infarct a piece of material (usually a blood clot) is formed in one place and then travels through the bloodstream to suddenly lodge in and occlude a blood vessel supplying the brain." [**5**]

Hemorrhagic Stroke

Rupture of a blood vessel and bleeding into the brain, spinal cord, or adjacent structures constitutes the cases of hemorrhagic stroke [**7**]. Tissue adjacent to bleeding exhibits neuronal injury, edema, and an inflammatory reaction. The hemorrhage damages adjacent brain tissue and provokes the development of vasogenic and cytotoxic edema [**7**]. Categories of hemorrhagic stroke include aneurysmal hemorrhage and vascular malformation [**7**]. Intracranial hemorrhage is the most common presentation of a ruptured aneurysm [**7**].

b. Saccular (Berry) Aneurysms

These are balloon-like structures outpouchings from the vessel wall, which typically have a neck connecting it to the parent vessel and a fragile dome that has relatively thinner wall and most likely location for aneurysmal rupture [**5**,**7**]. Saccular aneurysms generally arise at the junctions of arteries because of hemodynamic stresses [**7**]. A graphical illustration of a brain aneurysm is provided in Figure 1.8 depicting shape of an aneurysm and a coil placed into it to block blood perfusion into it. A real 3-D angiographic image of a brain aneurysm is given in Figure 1.9.

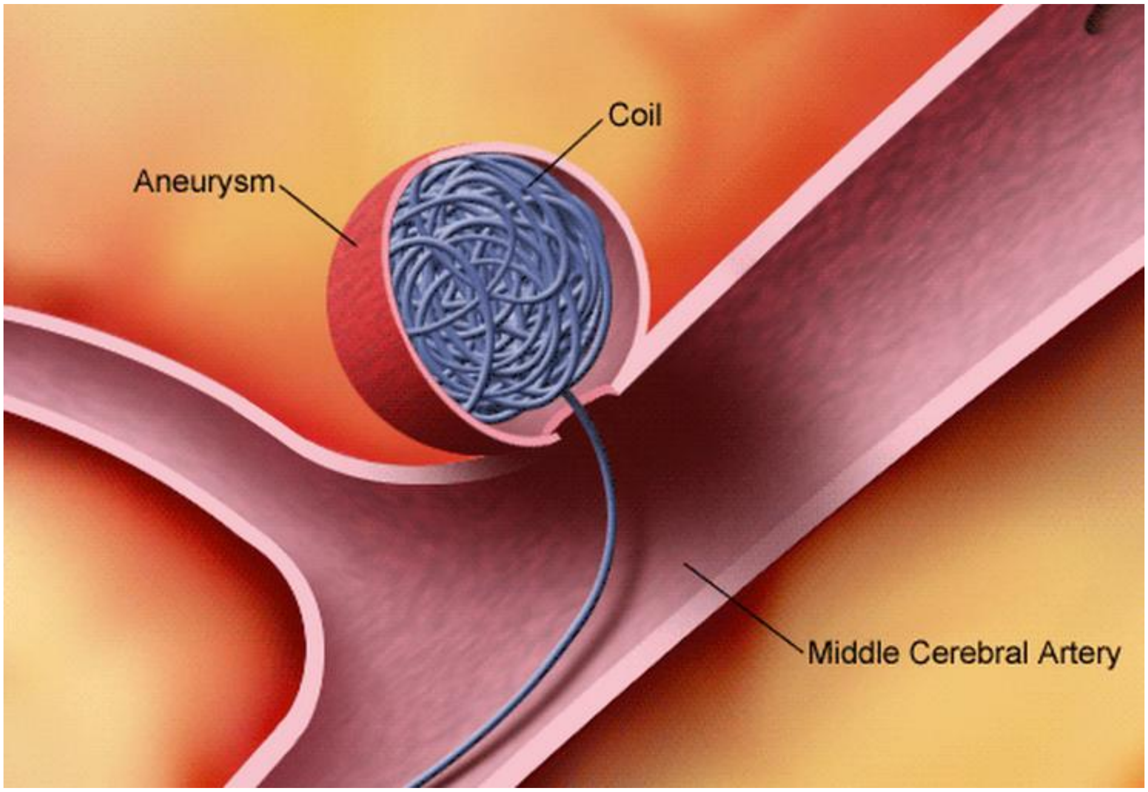

Figure 1.8 - A graphical illustration of a saccular brain aneurysm. To prevent rupture of aneurysms, a coil is placed into it so that blood supply into the aneurysm is blocked **[**10**]**.

Figure 1.9 - A real 3-D image of cerebral vessels, where the arrow points at a saccular aneurysm **[**11**]**.

"Approximately 85 percent of the saccular aneurysms are located in the carotid circulation with the region of the anterior communicating artery, the origin of the posterior communicating artery, and the bifurcation of the middle cerebral artery being the most common sites" [**7**,**5**].

"In general, the risk of bleeding is associated with the size of saccular aneurysm. The risk of rupture is relatively low when an aneurysm is <5 mm in diameter. The average size of ruptured aneurysms is approximately 6-8 mm. Unruptured aneurysms >10 mm in diameter have the highest risk for bleeding." [**7**]

Factors associated with rupture of intracranial aneurysm are arterial hypertension, smoking, heavy alcohol use, oral contraceptive use, sypathomimetric drug use/abuse [**7**].

c. Arteriovenous Malformation

Vascular malformations are an important cause of intracranial hemorrhage. The frequency of hemorrhage due to a vascular malformation peaks in the fourth decade of life [**7**].

The most common form of vascular malformations is the arteriovenous malformation (AVM) [**7**]. AVMs are congenital abnormalities in which there are abnormal direct connections between arteries and veins [**5**], including arterial elements, a node of dysplastic vessels, which is intermixed with gliotic brain tissue, and dilated, arterialized veins [**7**]. Figure 1 shows an x-ray image of an AVM, while Figure 2 shows its image after treatment.

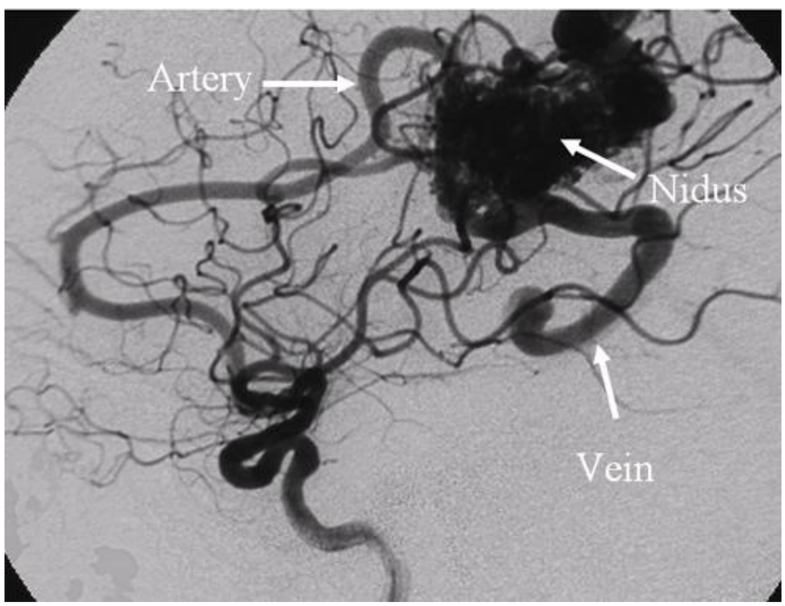

Figure 1.10 - The AVM is seen as a dense collection of vessels (the nidus) that connect the arteries directly to the veins without an intervening capillary system **[**12**]**.

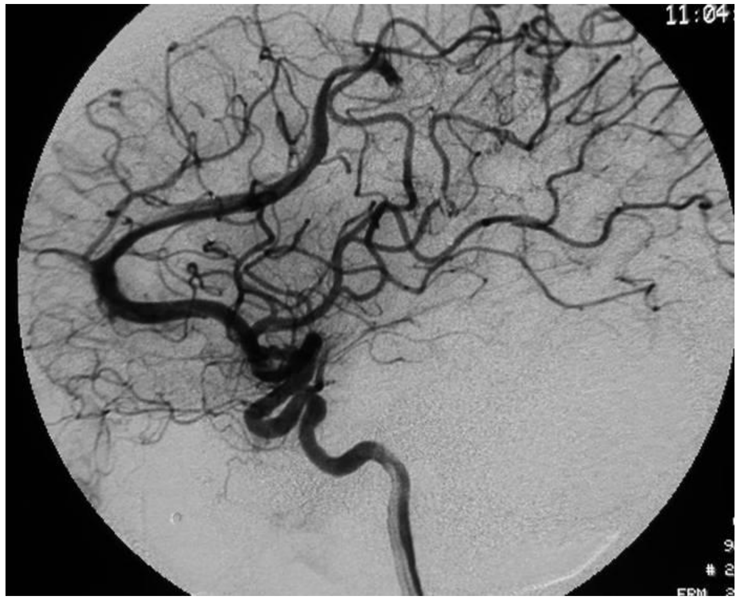

Figure 1.11 - After Treatment: the AVM is cleared, allowing better circulation **[**12**]**.

Determining the branches feeding an AVM has critical importance for therapeutic purposes. Multiple arterial branches arising from both the carotid and vertebrobasilar circulations may be found. Branches of the external carotid artery also can supply the malformation. Hemorrhage may be more frequent among those AVMs that are small or located deep in the cerebral hemispheres [**7**].

1.4.3. Cerebrovascular Imaging

When visualizing lesions of the cerebral blood vessels, neuroangiography comes into consideration rather than obtaining information about surrounding structures. Angiography provides optimum information about the lesions such as narrowings like atherosclerotic plaques, aneurysms, and arteriovenous malformations [**5**].

Although less invasive imaging techniques are developed more in the last decade by means of blood vessel visualization and flow assess, conventional catheter-based neuroangiography is still the gold-standard in evaluation of various intracranial and extracranial vascular abnormalities [**5**]. For most purposes, none of those less invasive techniques achieves the sensitivity and specificity of conventional catheter-based neuroangiography [**5**].

For many purposes, one of less invasive techniques, namely doppler ultrasound, magnetic resonance angiography, and spiral computed tomography angiography, is used first. If the diagnosis remains unclear, conventional angiography is used [**5**]. It is also important to note that conventional angiography is used also for therapeutic purposes [**5**].

a. Doppler Ultrasound

This is used to measure flow and lumen diameter of large blood vessels in the head and neck. Doppler ultrasound is most useful for assessing the proximal portions but not for distal branches [**5**]. This technique cannot detect aneurysms [**5**].

b. Magnetic Resonance Angiography (MRA)

MRA can visualize the major vessels while it cannot visualize the distal branches. MRA is mainly useful for detecting arterial blood flow caused by atherosclerotic narrowing, thrombosis or dissection, and for detecting some aneurysms [**5**].

c. Spiral Computed Tomography Angiography (CTA)

Intravenous contrast agent is rapidly injected and blood vessel images are quickly obtained by implementation of helical CT scanning techniques. While CTA can sometimes provide additional information compared to MRA, it is noteworthy that CTA is applicable for patients with MRA contraindication (such as patients with pacemakers) [**5**].

d. Catheter Angiography

Although MRA and CTA are used for the initial diagnosis, catheter angiography is used for planning cerebrovascular surgery and endovascular therapy in diseases such as stroke, atheromatous stenosis, aneurysms, vascular malformations, and vascular tumors [**13**]. During this technique, guidewire and catheter are inserted into the patient, usually in the femoral artery under local anesthesia, and threaded up the aorta under continuous x-ray guidance [**5**] (Figure 1.12). Guidewire leads, catheter proceeds after it by gentle manipulation to avoid vasospasm, dissection, and catheter-related emboli [**13**]. Contrast material is then injected into the carotid and vertebral arteries on both sides, and sequential images of vessels are obtained at different times [**5**]. On the other hand, catheter angiography serves for therapeutic applications. Brain aneurysms and arteriovenous malformations can be clotted off and rendered harmless by filling them via the angiography catheter [**5**].

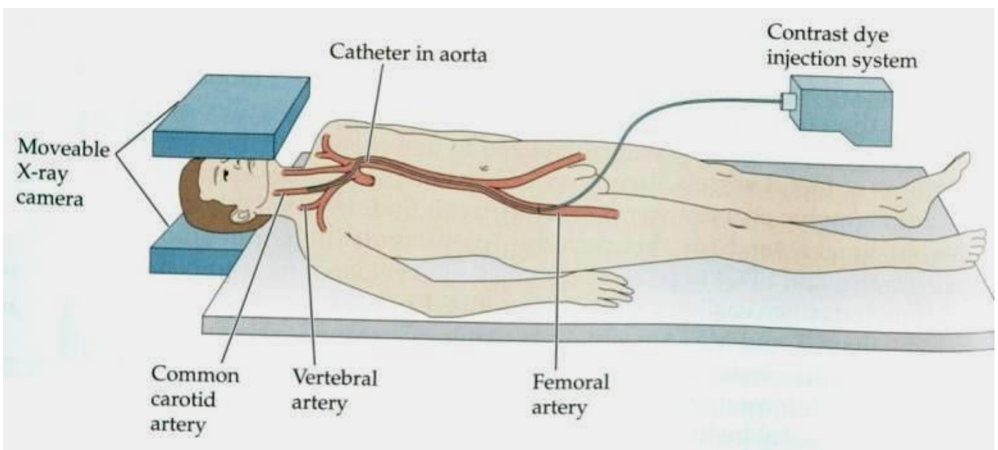

Figure 1.12 - Angiography setup **[**5**]**.

1.5. Problem Definition

To obtain the following information in an angiography suit, an endovascular radiologist uses visual inspection, which leads to more time and contrast agent consumption and x-ray dose:

- The path to reach a pathology, such as an aneurysm or an AVM,
- The feeders of an AVM,
- The branches going in and out of an aneurysm,
- The network under risk of embolization due to the operation.

The problem of proposing an algorithm to extract vascular network connected to a user-defined point in a user-defined direction reduces to 3-D vascular connectivity tracking, which includes

- 3-D vessel tracking,
- 3-D skeletonization,
- 3-D pruning,
- 3-D junction detection,
- 3-D volume growing.

The proposed algorithm could be applied to

- Highlighting the path reaching to an aneurysm,
- Highlighting the branches connected to an aneurysm,
- Determining the arteries supplying blood perfusion to an AVM,
- Foreseeing the network distal to the point of operation, where is under risk of embolization, hence of occlusion.

CHAPTER 2

THEORY

2.1. Literature Review

2.1.1. Vessel Tracking

In medical image processing literature, tracking concept is mostly taken into account for vessel segmentation applications, i.e. to differentiate between vessel and non-vessel points in a given image. Tracking the points, which are known to belong to a vessel, increases contrast so that separates the vessels from the adjacent tissue and noise signal. This section provides a general overview on vessel tracking methods. Those methods cover different applications on different imaging techniques, image dimensions and anatomical structures.

Reuze, Coatrieux, Luo, and Dillesenger propose a method to track 3-D MRA images and quantitatively analyze blood vessels in them [**14**]. Based on 3-D geometric moments, user-defined seed points are tracked, local diameter and orientation are computed. This method is not capable of handling junctions, it does not work on "forking situations" and require user interaction to continue.

Method proposed by Klose, Petersen, and Martos is also applied to 3-D MRA images and employs connectivity to track the vessels [**15**]. The authors aim at visualizing small vessels, which are not visible due to superposition of background signal. Algorithm starts with an interactively defined seed point and determines the voxels connected to one another, starting from the seed. At the branching points, the user interaction is required to set an additional seed point.

A cerebral vessel extraction method from MRA images is presented by Luo, Lee, Ma, Aziz, and Nowinski [**16**]. Robust intensity searching and region growing algorithms are introduced for extraction, connectivity tracking is used to make sure that extracted branches are connected to vertebral and carotid arteries.

Kim and Park propose a connectivity-based local adaptive thresholding algorithm for carotid artery segmentation from MRA images [**17**]. Segmented carotid image is used for stenosis quantification and virtual endoscopy applications.

Collorec and Coatrieux propose a vectorial tracking algorithm to extract vascular structures in 2-D catheter angiography images [**18**]. The algorithm can fail to detect vessel portions if severe stenosis occurences exist.

Kutka and Stier present an algorithm for vessel segmentation, which is applied to highly noisy 3-D catheter angiography images, extracted cerebral vessels and their physical properties like intensity and diameter [**19**]. Similarly, Quek and Kirbas extract vascular structures from 2-D catheter angiography images [**20**]. These authors employ a wave propagation and traceback mechanism to label pixels with the likelihood that it is within a vessel. Felkel, Wegentkittl, and Kanitsar introduce a vessel tracking method for peripheral 3-D CTA datasets [**21**]. This work is dedicated to detect the main vessels in the leg and locate the stenoses. [**22**], and [**23**] cover further reviews on vessel extraction techniques and algorithms, including vessel tracking methods.

While none of the above mentioned vessel tracking works introduce any junction detection method, there exists vessel tracking articles that also propose methods on junction detection.

Liu and Sun recursively track vascular networks in a 2-D angiogram, they iterate on detecting branches and deleting those detected branches [**24**]. The algorithm starts with identifying the network starting from a user-defined point in a user-defined direction. Initially, it detects a branch and deletes that branch to prevent double tracking. Then, junctions on the branch are detected by using matched filtering along both edges of the vessel. These junctions are used as starting points in the initiation of later recursions. Since the method is proposed for detecting vascular network connected to a user-defined point in a specific direction, this method is not directly applicable to our problem because we are after detecting the networks in 3-D datasets. However, perspectives on detecting-deleting and using junctions as new starting points are implemented in our work.

Zhou, Hadjiiski, Sahiner, Chan, Patel, Cascade, Kazerooni, and Wei propose an algorithm for computerized detection of pulmonary embolism in 3-D CT images [**25**]. Within that algorithm, they implement a bifurcation analysis in 3-D images together with vessel tracking and segmentation techniques. Unfortunately, their article did not directly contributed to our method since the bifurcation analysis method is not clarified and no results regarding bifucation analysis are provided.

Proposal of Bullitt, Aylward, Liu, Stone, Mukherji, Coffey, Gerig, and Pizer on largely automated detection of connected 3-D cerebral vascular structures include segmentation and skeletonization vessels in 3-D MRA images [**26**]. Although it seems that they propose a solution to our problem, their method has some severe disadvantages. Their method does not detect trifurcations and higher-order junctions, and it connects separate branches as if they have a junction. Furthermore, no result on distal vessel tracking is provided in the article, while revealing the distal connections of a vascular network is a primary concern of us.

In literature, two outstanding articles exists which proposes methods on extracting vessel network connected to a specific point, working on 3-D angiographic images. Carrillo, Hoyos, Davila, and Orkisz propose an algorithm, which is expected to extract the axes of the vascular network connected to a user-defined seed point in 3D medical images [**27**]. The algorithm recursively tracks branches by sliding a sphere along the vessels, and detects bifurcations by analyzing the binary connected components on the surface of the sphere. Unfortunately, this algorithm fails in tracking the vessels, the continuity of which is affected by severe stenoses and this disadvantage is not negligible. Furthermore, the algorithm is dependent on differences of size and intensity between a branch and a sub-branch connected to it. Since the algorithm assumes similar intensities and the opposite can highly occur in real images, it is highly possible that the algorithm ignores some junctions.

In 2001, Flasque, Desvignes, Constans, and Revenu present an iterative vessel tracking method [**3**]. Starting from a user-defined seed point, weighted center of mass in a specific local volume is computed, new seed point and tracking direction are obtained [**3**]. Iterative implementation of this computation yields a branch, which is connected to the user-defined seed point in the user-defined direction. The tracking method introduced in this article is the one, which is applied within our work. On the other hand, even if the authors have implemented a junction detection method, it is not well-defined and it is stated to fail if junction angles are 10 degree or less and 170 degree or more.

Brief Overview on Vessel Tracking Literature

Although there is a vast amount of studies in literature, these studies have severe disadvantages in terms of 3-D branch tracking. They either cannot handle junctions, require further user interaction, do not regard connectivity to a specific point, crashes if stenosis exists, or cannot detect trifurcations and such higher order junctions. These studies are mostly dedicated to 2-D image processing.

Two distinguished studies became inspiring in terms of single branch tracking method [**3**] and preventing double tracking vascular branches [**24**]. Methods and perspectives proposed in these articles are applied to our algorithm.

2.1.2. Skeletonization

Skeletons are region-based shape descriptors which summarize the general form of objects/shapes. An illustrative definition of the skeleton is given using the prairie-fire analogy: the object boundary is set on fire and the skeleton is formed by the loci where the fire fronts meet and extinguish each other [**28**].

Skeletonization methods can be grouped into four main classes, which are thinning methods, voronoi-based methods, distance-based methods, and general-field methods [**28**,**29**]. Voronoi-based methods are expressed in [**28**], while detailed information on distance-based methods is provided in [**28**] and general-field methods in [**28**]. From those classes, thinning method guarantees connectivity [**29**] and is the mostly preferred method for skeleton extraction procedures [**30**].

Thinning can be considered as an iterative peeling-off process. During a thinning operation, *simple* voxels within the boundary of an object are identified and removed [**29**,**31**]. Starting from the outermost layer, the object is eroded layer by layer at each iteration until only the skeleton of the object remains [**28**]. The entire process is terminated when no more voxel can be removed.

Skeletonizing the vascular structure is necessary in our case to detect the junctions and compute the angles, which the direction of new tracking initiations. These purposes lead us to implement a thinning method to extract vascular skeleton, which is capable of preserving both connectivity and topology [**28**].

Thinning algorithms can be divided into two with respect to the resulting skeleton. *Curve-thinning* algorithms extract medial lines/center lines, while surface-thinning algorithms result with medial surfaces of objects [**28**,**32**]. Topological thinning methods are further divided into two subgroups as being sequential or parallel, regarding the implementation of iterations. Thinning algorithms are mostly parallel because “the fire front propagation is parallel by nature” [**33**].

Main concern of thinning operations is about determining a voxel whether it is removable or not. A *simple point* is a voxel that the topology does not change and connected components stay still connected even after the voxel is removed out of the object. There exists many different discussions on defining a simple point in 2-D. On the other hand, simple point definition in 3-D is still complicated, since new topological possibilities arise.

Bezerra and Leite gather and summarize different concepts for characterizing simple points [**34**]. They also present some equivalences between simple point characterization methods for 3-D image skeletonization. The distinguished methods are clearly defined in Section 2.2.2.

Besides summarizing simple point definition theorems, Pan and Klette propose a 3-D skeletonization method based on *non-simple voxe*l identification [**31**]. A 3-

D sequential 6-subiteration thinning algorithm [**30**] is tested for simple symmetric 3D objects. A large number of different combinations of preprocessing steps are provided.

Reinders, Jacobson, and Post approach to the subject from another perspective and describe methods on post-processing of skeletonized 3-D images [**29**]. The authors focused on voxel graph construction from the skeleton, graph simplification, and shape reconstruction from graphs.

While Gonzalez and Woods describe perspectives on pruning the raw skeleton [**35**], Palagyi, Tschirren, and Sonka propose a method for quantitative assessment of intrathoracic airway trees, the authors also present a perspective on branch-point identification [**36**]. These perspectives are expressed in Section 2.2.3 and Section 2.2.4, respectively. Pruning supports junction-detection method in terms of eliminating false junctions.

Two articles present 3-D medial axis thinning algorithms, which are applicable to our purposes. While Palagyi et al. present a method to determine some characteristics of removable points [**37**], while Lee, Kashyap, and Chu present an Euler characteristic based method to preserve connectivity and topology features of the original image [**4**]. We have implemented a combination these two methods, which is discussed in details in Section 2.2.2.

Brief Overview on Skeletonization

Literature contains useful studies on skeletonization in terms of characterizing simple points, non-simple voxel identification, 3-D sequential 6-subiteration thinning algorithm for simple symmetric objects, and post-processing of skeletonized 3-D images, focusing on shape reconstruction from skeleton. References [**35**], [**36**], [**37**], and [**4**] present inspiring methods and perspective on pruning operation, junction identification, identification of border-points and end-points, and topology and connectivity preservation during thinning operation, respectively.

2.1.3. Junction Detection

Detecting junctions has a vital importance to solve 3-D vessel connectivity tracking to locate bifurcations and trifurcations and connect the distal sub-branches to the main network. Literature presents a wide range of junction detection algorithms, mostly applied on 2-D images. Among them, 2-D retinal image processing is a strong focus of interest in the field of medical imaging: Blood vessel detection and tracking algorithms exist for the ocular fundus images. There are vessel junction detection algorithms generated for this purpose.

Chutatape, Zheng, and Krishnan implement a branching detection strategy which is simultaneously executed with vessel tracking algorithm [**38**]. It cannot detect a junction if the angle between the main branch and a sub-branch is less than 30^0 or greater than 90^0. Tao and Gao propose a perceptual organization based method for junction detection in retinal images [**39**]. The method proposed by Quelhas and Boyce includes edge detection and searching for branches along the edges [**40**]. Similarly, Leandro, Cesar, and Costa detect junctions by determining continuity along crossings [**41**]. However, since these algorithms are after 2-D junction detection, they are not directly applicable to our case.

Among the methods proposed for junction detection in 3-D images, Zhou, Chang, Metaxas, and Axel present a bifurcation detection method [**42**]. This method uses AdaBoost learning method with specially designed filters on cross-sections of vessels to reveal junctions. Friman, Hindennach, Kühnel, and Peitgen's method on branch detection is based on a spectral clustering algorithm [**43**]. Finally, Fridman, Pizer, Aylward, and Bullitt detect bifurcations by using an affine-invariant corner detector [**44**]. While this last method is likely to generate useful results for our case, we considered to detect junctions on skeletonized central lines, which could yield more accurate and exact localization of junctions. The latter method could also help determining the directions of sub-branches with respect to the junction point.

Brief Overview on Junction Detection

While many junction detection studies can be found in the literature, they are mostly far away from being applicable onto our problem. In [**36**], authors present outstanding methods and perspectives on junction detection by examining the 26-neighborhood of a voxel. Their straightforward and time saving method is applied within our algorithm.

2.1.4. Region Growing

As tracking and skeletonization algorithms are applied on a 3-D image of vessels, the resulting image carries compact information on centers of mass and skeletons of the vessels. The image carries much less non-zero voxels, full shapes of vessels are not evident. Full shapes are required at the final image, so that the shape information must be recovered. Region growing concept is put into service to achieve the recovery.

Gonzalez and Woods provide a clear region growing description in [**35**]. However, this description is given for 2-D images, while we require to grow regions in 3-D images. In order to gain familiarity with the concept, theoretical background of region growing is discussed in details below.

2-D region growing procedure groups pixels or subregions into larger regions based on predefined criteria. The process is initiated with a set of "seed" points and neighboring pixels that have properties similar to the seed (such as specific ranges of gray level or color) append to these seeds [**35**].

Selecting a set of one or more starting points often can be based on the nature of the problem. The selection of similarity criteria depends on the features of the problem under consideration and the type of image data. When the images are monochrome as in our case, region analysis must be carried out with a set of descriptors based on gray levels and spatial properties [**35**].

Descriptor selection carries special importance on keeping away from misleading results, connectivity or adjacency information is used to achieve coherency in the region-growing process [**35**].

Another problem in region growing is the formulation of a stopping rule. Basically, growing a region should stop when no more pixels satisfy the criteria for inclusion in that region [**35**]. While keeping in mind that voxels belonging to vessels have a non-zero gray level intensity and non-vessel voxels' intensity is zero, gray level information that voxels carry is the main criterion that we check to stop growing.

Based on the method proposed by Gonzalez and Woods, we have extended the 2-D region growing method to 3-D and presented a new method, namely *volume growing*. Implementation of method is described in Section 2.2.5.

2.2. Methods

2.2.1. Tracking Single Vascular Branches

Vessel tracking method is an iterative process, which is initiated by user: Method gets the user-defined initiation point P_0 and user-defined initiation direction D_0, and produces an order set of points $\{P_i\}$ and correspondingly $\{D_i\}$ as the expected outputs. $\{P_i\}$ and $\{D_i\}$ are computed step-by-step in a local volume around the previous point P_{i-1} in previous D_{i-1} direction [**3**].

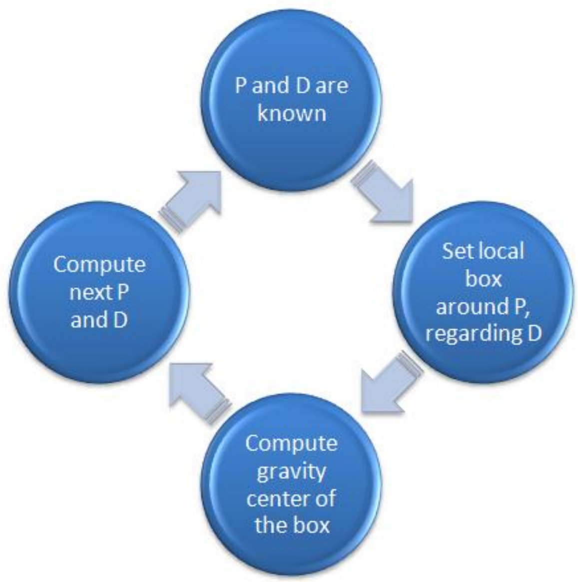

Figure 2.1 - Single vascular branch tracking iteration. The iteration is terminated when intensity of voxels go under a specified value.

a. Local Box and Its Gravity Center

Letting P_i be the current point and D_i be the current tracking direction, a box is created such that P_i is located in the center of its lower base, and D_i determines the box orientation with respect to a global coordinate system and P_i.

Let unitary vectors $D_{\perp 1}$, $D_{\perp 2}$ be two directions such that $D_i \perp D_{\perp 1} \perp D_{\perp 2} \perp D_i$, and let integer numbers of voxel l_i, m_i, and H_i be the dimensions of box [**3**].

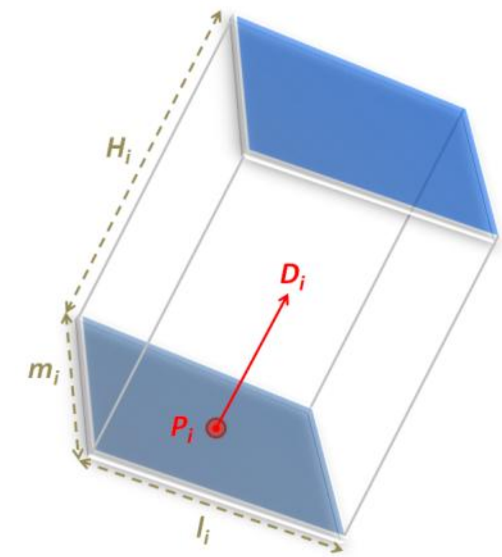

Figure 2.2 - Local box around a point $\boldsymbol{P_i}$ in the direction $\boldsymbol{D_i}$. $\boldsymbol{D_i}$ stays in the center of the box' base. The dimension of base is $\boldsymbol{l_i} \times \boldsymbol{m_i}$, while $\boldsymbol{H_i}$ is the height of box.

Assuming a local coordinate system with its origin at the center of the box and letting $\alpha \in [-l_i, l_i]$, $\beta \in [-m_i, m_i]$, $\gamma \in [-H_i, H_i]$, one can express 3-D coordinates of any voxel within the box with respect to the local coordinate system.

Let $X_{\alpha,\beta,\gamma} = P_i + \alpha \cdot D_{\perp 1} + \beta \cdot D_{\perp 2} + \gamma \cdot D_i$, and $A_{\alpha,\beta,\gamma}$ a weight associated with $X_{\alpha,\beta,\gamma}$.

Then, coordinates of the weighted gravity center B_i of the local box corresponding to P_i and D_i is given as [**3**]

$$B_i = \frac{\sum_{X_{\alpha,\beta,\gamma} \in V} A_{\alpha,\beta,\gamma} X_{\alpha,\beta,\gamma}}{\sum_{X_{\alpha,\beta,\gamma} \in V} A_{\alpha,\beta,\gamma}} .$$

The weight $A_{\alpha,\beta,\gamma}$ of each voxel is taken as its intensity in the 3-D image.

b. Computation of next point

3-D coordinates of the next point is given as [**3**]

$$P_{i+1} = \frac{(k_p P_i) + B_i}{k_p + 1} \;;$$

where k_P is a constant affecting the distance between two sequential points, hence acting on the sensitivity of the method. Setting $k_p = 0$ locates the next number P_{i+1} exactly at the gravity center B_i, while increasing k_p pulls P_{i+1} closer to the current point P_i.

c. Computation of next direction

The next direction of local box is given as [**3**]

$$\overrightarrow{D_{i+1}} = \frac{\overrightarrow{D_i}}{\left\|\overrightarrow{D_i}\right\|} + k_d\left(\frac{\overrightarrow{B_i - P_i}}{\left\|\overrightarrow{B_i - P_i}\right\|}\right);$$

where k_d is also a constant acting on the relation between two succeeding directions. Setting $k_d = 0$ fixes directions of all boxes to initial user-defined direction D_i. As k_d increases, box direction of the next point is aligned between the former box direction and the direction pointing at B_i from P_i. Therefore, greater k_d achieves better performance on tracking curvatures.

d. Termination of Iteration

As locations of points P_i get closer to the end of distal branches, voxels' intensity and, hence, contrast ratio dramatically decrease. The number $\sum_{X_{\alpha,\beta,\gamma} \in V} A_{\alpha,\beta,\gamma}$ is continuously observed: When its value gets lower than a user-defined threshold, tracking iteration is stopped.

2.2.2. Skeletonization

3-D skeletonization is an iterative process that successively deletes some special points carrying specific characteristics. A *simple point* definition is given to assure that the connectivity and topology features of the original 3-D object are preserved. The process is terminated when no more point can be deleted from the image.

Main Definitions

Let p a point in the 3-D digital space $\mathbb{Z}^3$ [**37**].

Let us denote $N_j(p)$ (for j = 6, 18, 26) the set of points j-*adjacent* to a point p. The sequence of distinct points $\langle x_0, x_1, \ldots, x_n \rangle$ is a j-*path* of length $n \geq 0$ from point x_0 to point x_n in a non-empty set of points X if each point of the sequence is in X and x_i is j-*adjacent* to x_{i-1} for each $1 \leq i \leq n$. (Note that a single point is a j-path of length 0.) [**37**]

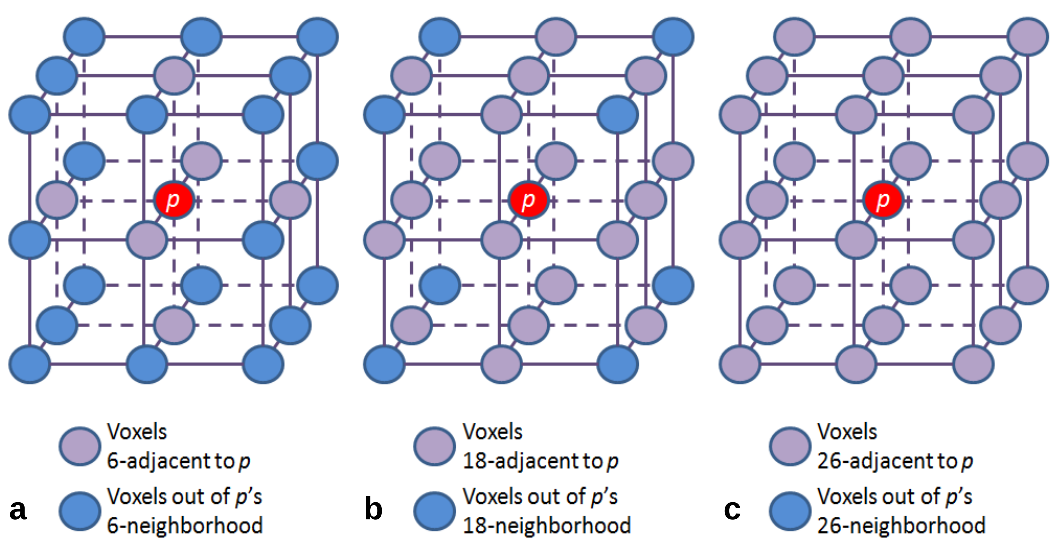

Figure 2.3 - Illustration of voxels which are *n*-adjacent to $\boldsymbol{p}$.
a) *n* = 6, b) *n*=18, c) *n*=26

Two points are j-*connected* in the set X if there is a j-path in X between them.
A set of points X is j-*connected* in the set of points $Y \supseteq X$ if any two points in X are j-connected in Y [**37**].

The *3-D binary* (m, n) *digital picture* P is a quadruple $P = (\mathbb{Z}^3, m, n, B)$ [**37**]. Each element of $\mathbb{Z}^3$ is called a *point* of P. Each point in $B \subseteq Z^3$is called a *black point* and value 1 is assigned to it. Each point in $\mathbb{Z}^3 \backslash B$ is called a *white point* and value 0 is assigned to it. Adjacency m belongs to the black points and adjacency n belongs to the white points. A *black component* (or *object*) is a maximal m-connected set of points in B. A *white component* is a maximal n-connected set of points in $B \subseteq \mathbb{Z}^3$. We are dealing with (26, 6) points [**37**].

There exists exactly one component of $\mathbb{Z}^3 \backslash B$ that contains the boundary points of $\mathbb{Z}^3$. The other components of $\mathbb{Z}^3 \backslash B$ are completely surrounded by B, and are called *cavities*. Difference between a cavity and a *hole* is that a hole is not completely surrounded by B. A 3-D hole can be considered as the tunnel in a torus [**4**].

A black point in a (26, 6) picture is called *border point* if it is 6-adjacent to at least one white point [**37**].

A border point p is *simple* if and only if removing it does not change the number of connected objects of both B and $\mathbb{Z}^3 \backslash B$ [**4**].

Theorem: Simple Point

Black point p is *simple* in picture $(\mathbb{Z}^3, 26, 6, B)$ if and only if all the following conditions hold [**37**]:

1. The set $N_{26}(p) \cap (B \backslash \{p\})$ is not empty (i.e., p is not an isolated point);

2. The set $N_{26}(p) \cap (B \setminus \{p\})$ is 26-connected (in itself);
3. The set $(\mathbb{Z}^3 \setminus B) \cap N_6(p)$ is not empty (i.e., p is a border point);
4. The set $(\mathbb{Z}^3 \setminus B) \cap N_6(p)$ is 6-connected in the set $(\mathbb{Z}^3 \setminus B) \cap N_{18}(p)$

Palagyi et al. [**37**] propose a thinning algorithm, which starts iterations by determining the border and non-end-points in each direction separately. Note that a point is not an end point if it has at least two black points, and directions are north, south, east, west, up, and down.

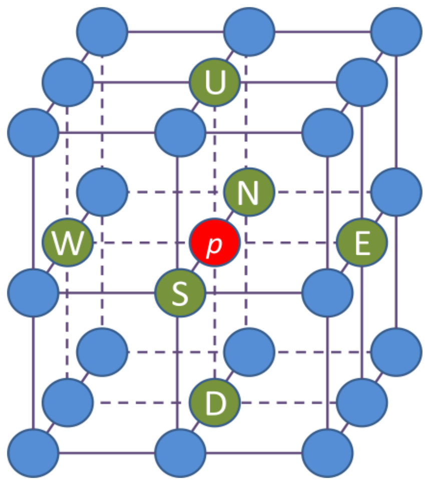

Figure 2.4 - Special neighbors of $\boldsymbol{p}$. These voxels are used to determine what type of a border point $\boldsymbol{p}$ is. If *N*=0, $\boldsymbol{p}$ is a border point of type-N. If *S*=0, $\boldsymbol{p}$ is a border point of type-S. If *E*=0, $\boldsymbol{p}$ is a border point of type-E. If *W*=0, $\boldsymbol{p}$ is a border point of type-W. If *U*=0, $\boldsymbol{p}$ is a border point of type-U. If *D*=0, $\boldsymbol{p}$ is a border point of type-D.

The algorithm checks if 2nd and 4th conditions of the theorem are satisfied by determined border and non-end-points. This checking procedure assures connectivity and topology preservation of the algorithm. On the other hand, also Lee et al. [**4**] present two different methods on achieving connectivity and topology preservation.

Euler Characteristic to Preserve Connectivity and Topology

One connectivity and topology preserving method introduced in [**4**] is based on Euler characteristic and Euler invariance computation of 26-neighborhood of a border and non-end-point, while the latter method proposes a labeling algorithm to determine the number of 26-connected objects in the neighborhood.

As the theoretical background of Euler characteristic based method is described below, reader is encouraged to refer to [**4**] to reach the detailed description of labeling algorithm.

Then, the 3-D Euler characteristic $\chi(B)$ is defined by the global formula

$$\chi(B) = O(B) - H(B) + C(B);$$

where, $O(B)$, $H(B)$, and $C(B)$ are the number of connected objects, holes, and cavities of B, respectively [**4**].

Lobregt et al. [**4**] divide $N_{26}(p)$ into eight overlapping $2 \times 2 \times 2$ octants, denoted as $N^2(p)$. The corners of an octant correspond to a digit of an 8-digit binary number. The point p is located at the position 8 and corresponds to the least significant bit, while position 1 corresponds to the most significant bit.

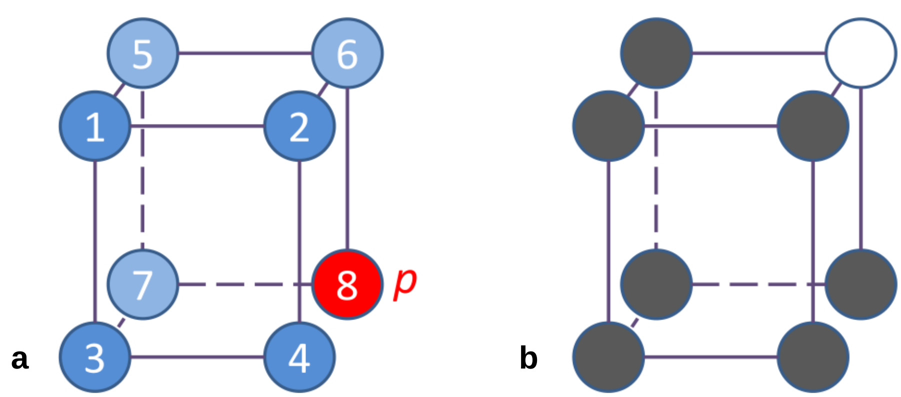

Figure 2.5 - a) A $2 \times 2 \times 2$ octant, $\boldsymbol{N^2(v)}$; b) An example octant with a configuration corresponding to binary 11111011. Note that black points have value 1, and white points have value 0.

The Euler characteristic is computed by directly summing the individual contributions of each octant. The advantage of using this approach is that there are only $2^8 (= 256)$ possible configurations of each octant. Contribution of any octant configuration on Euler characteristic can be calculated and saved. To reduce the complexity of Euler characteristic calculation, the authors designed a look-up table [**4**], increasing the efficiency of computation Table 2-1. Table shows the Euler characteristic equivalents corresponding to any octant configurations: Once the equivalent number of an octant is calculated, its corresponding Euler characteristic can be directly taken from the table.

Euler characteristic is computed only for those border and non-end black points, i.e. the least significant digit is always 1. Hence, the table includes Euler characteristics only for configurations corresponding to odd values.

Table 2-1 - Euler table for preserving Euler characteristic.

Octant's numeric equivalent	Euler characteristic for 26-connected objects	Octant's numeric equivalent	Euler characteristic for 26-connected objects	Octant's numeric equivalent	Euler characteristic for 26-connected objects	Octant's numeric equivalent	Euler characteristic for 26-connected objects
1	1	65	-3	129	-7	193	-3
3	-1	67	3	131	-1	195	3
5	-1	69	-1	133	-1	197	-1
7	1	71	1	135	1	199	1
9	-3	73	1	137	-3	201	1
11	-1	75	3	139	-1	203	3
13	-1	77	-1	141	-1	205	-1
15	1	79	1	143	1	207	1
17	-1	81	-1	145	-1	209	-1
19	1	83	1	147	1	211	1
21	1	85	1	149	1	213	1
23	-1	87	-1	151	-1	215	-1
25	3	89	3	153	3	217	3
27	1	91	1	155	1	219	1
29	1	93	1	157	1	221	1
31	-1	95	-1	159	-1	223	-1
33	-3	97	1	161	-3	225	1
35	-1	99	3	163	-1	227	3
37	3	101	3	165	3	229	3
39	1	103	1	167	1	231	1
41	1	105	5	169	1	233	5
43	-1	107	3	171	-1	235	3
45	3	109	3	173	3	237	3
47	1	111	1	175	1	239	1
49	-1	113	-1	177	-1	241	-1
51	1	115	1	179	1	243	1
53	1	117	1	181	1	245	1
55	-1	119	-1	183	-1	247	-1
57	3	121	3	185	3	249	3
59	1	123	1	187	1	251	1
61	1	125	1	189	1	253	1
63	-1	127	-1	191	-1	255	-1

As an example, the octant configuration given in Figure 2.2 corresponds to binary number 11111011, which is decimal number 251. Euler characteristic for this octant configuration's numeric value is given in Table as 1, regarding 26-connected objects.

Euler invariance of $N_{26}(p)$ is then checked to examine if Euler characteristic changes after removal of a black point. A black point p within $N_{26}(p)$ must be invariant in the sense of Euler characteristic to assure topology preserving property of the thinning operation. Euler invariance is satisfied if contributions of individual octants of $N_{26}(p)$ sum up to 0 [**4**].

We have replaced the connectivity and topology preservation method presented by Lee et al. with the method proposed by Palagyi et al., while keeping perspectives of Palagyi et al. on checking whether a point is isolated and a border point.

Let d_s denote the direction, where d_s can be one of North, South, East, West, Up, and Down. Each voxel of image within the frame consisting of white points is then examined if it is a simple point. A voxel can be removed if

- The voxel is a black point
- The voxel is a border point of type-d_s.
- The voxel is not an end-point
- The 26-neighborhood of the voxel is Euler invariant

This examination, and hence the skeletonization algorithm are depicted in Figure 2.6. The algorithm is implemented on each direction, i.e., d_s is set to North, South, East, West, Up, and Down separately.

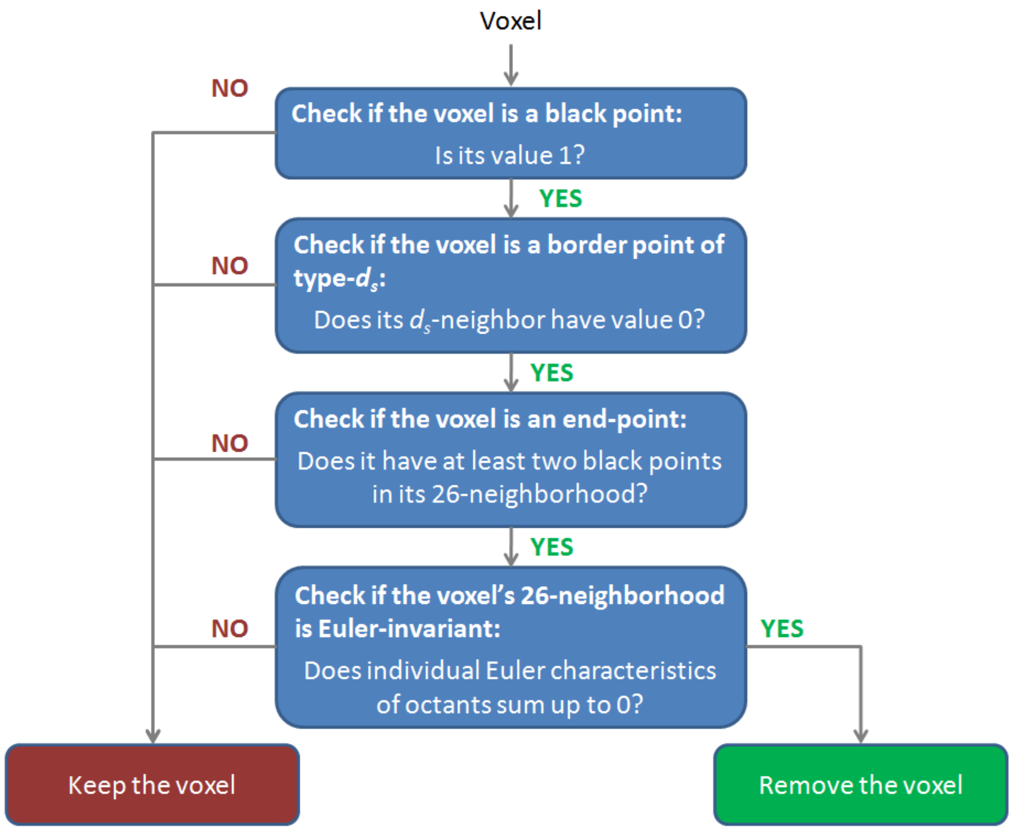

Figure 2.6 - Iterative procedure and decision-tree of skeletonization algorithm.

A preprocessing phase is required to execute the skeletonization procedure, 3-D vascular image is prepared for thinning within this phase. Since the skeletonization procedure assumes binary images, vascular image is first binarized. Then, to provide that the outermost voxels of the image are also examined, a frame consisting of white points is added on the image. This frame is required while constructing 26-neighborhoods of the outermost voxels. This preprocessing phase is depicted in Figure 2.7.

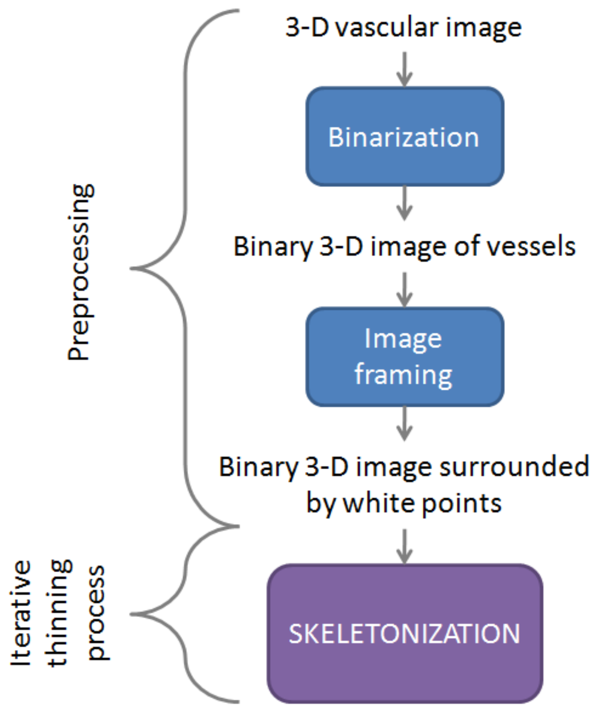

Figure 2.7 - Preprocessing phase, in which 3-D vessel images are prepared for skeletonization.

2.2.3. Pruning

Pruning is an integral part of skeletonization methods, since skeletonization methods inevitably leave twig-like parasitic components; pruning is a postprocessing method applied on skeleton to clean these twigs up.

As discussed in [**35**], single and end-points in the skeleton are iteratively removed. Since the twigs are shorter than the height of local box, and only skeleton portions longer than the height, a number of H_0 iterations are implemented.

2.2.4. Junction-Detection

Once skeleton of a 3-D image is extracted, each voxel in it satisfies exactly one of the following three conditions [**36**]:

1. The voxel is an end-point (i.e., it has only one black point in its 26-neighborhood).
2. The voxel is a line point (i.e., it has exactly two black points in its 26-neighborhood).
3. The voxel is a branch-point (i.e., it has three or more two black points in its 26-neighborhood).

Therefore, after skeletonization procedure is applied on an image, determining junctions in the output image is a straightforward process: The voxels having at least three black points in their 26-neighborhood are junctions.

2.2.5. Volume-Growing

Keeping in mind that region growing is a method concerning 2-D images; we propose a *volume-growing* method since 3-D images are to the subject. In 3-D, volumes are essential rather than regions.

First problem of volume growing is setting the seed points. During tracking and skeletonization procedures, many of the voxels are removed from the image. As a result, gravity centers and skeletons of vessels are obtained. Seed points should be selected in a manner so that they lead to recovery of vessels by appending previously eliminated voxels back to the seeds. Utilizing gravity centers P_i as seed points, one can grow volumes and recover vascular network connected to point P_0 in direction D_0.

Orientation of box around P_i, correspondingly D_i, and box dimensions are known for all gravity centers. Setting the same boxes around P_i again, and recovering the vessel voxels within those boxes result with recovery of tracked vessels. Therefore, the problem of recovering tracked vessel network reduces to recovering removed vessel voxels in local boxes.

Starting from the lowest slice of box, where P_i are present, region growing method described by Gonzalez and Woods [**35**] is implemented within all slices of the box. After setting P_i as the seed point, vessel voxels positioned in that box are appended to it by preserving connectivity.

Within a box, voxels adjacent to P_i are examined in terms of gray-scale intensity: Adjacent voxels having a non-zero intensity are appended to the seed, while adjacent voxels with zero intensity are left. Next, adjacencies of the appended voxels are examined in the same manner. This examination procedure is terminated when no more voxels exist which are adjacent to either P_i or latter appended voxels. This means that P_i and appended voxels form an island, surrounded by white voxels. The procedure is illustrated in Figure 2.8.

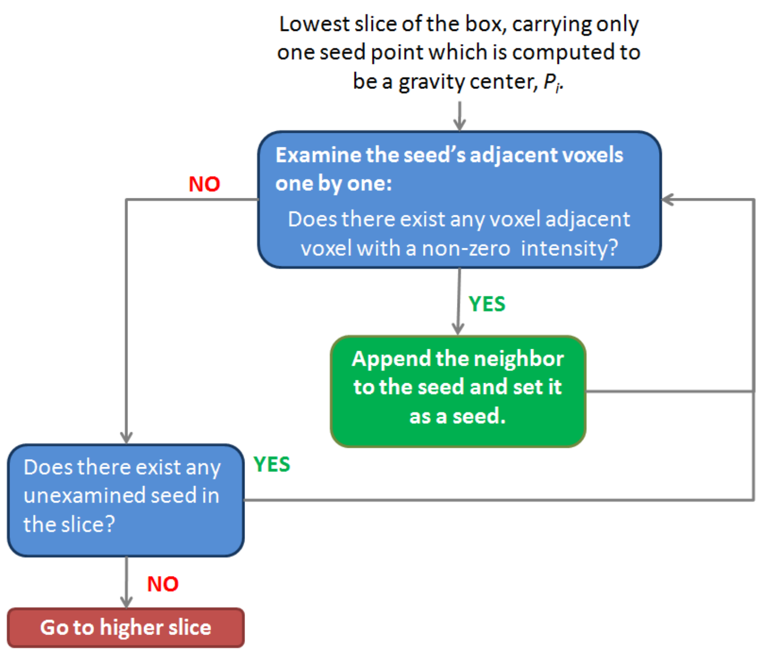

Figure 2.8 - Region growing process in the lowest slice of a local box.

Once region growing in a slice is terminated, one higher slice is examined: Vessel voxels within that slice, which are adjacent to the appended voxels in the lower slice are the seeds for the next examination. The entire process is repeated until the highest slice is examined as it is shown in Figure 2.9. Entire volume growing process is illustrated in Figure 2.10.

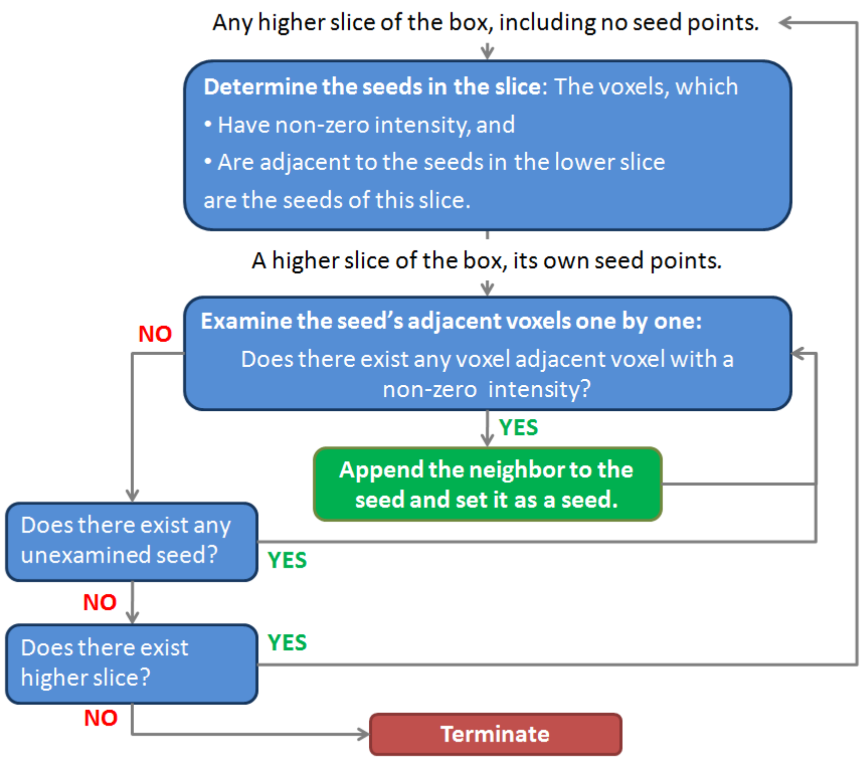

Figure 2.9 - Region growing process in the higher slices of a local box.

The advantage of this approach is that, while preserving connectivity, it also ignores vessel portions present within the box but belong to another branch. Therefore, branches with portions in boxes are excluded.

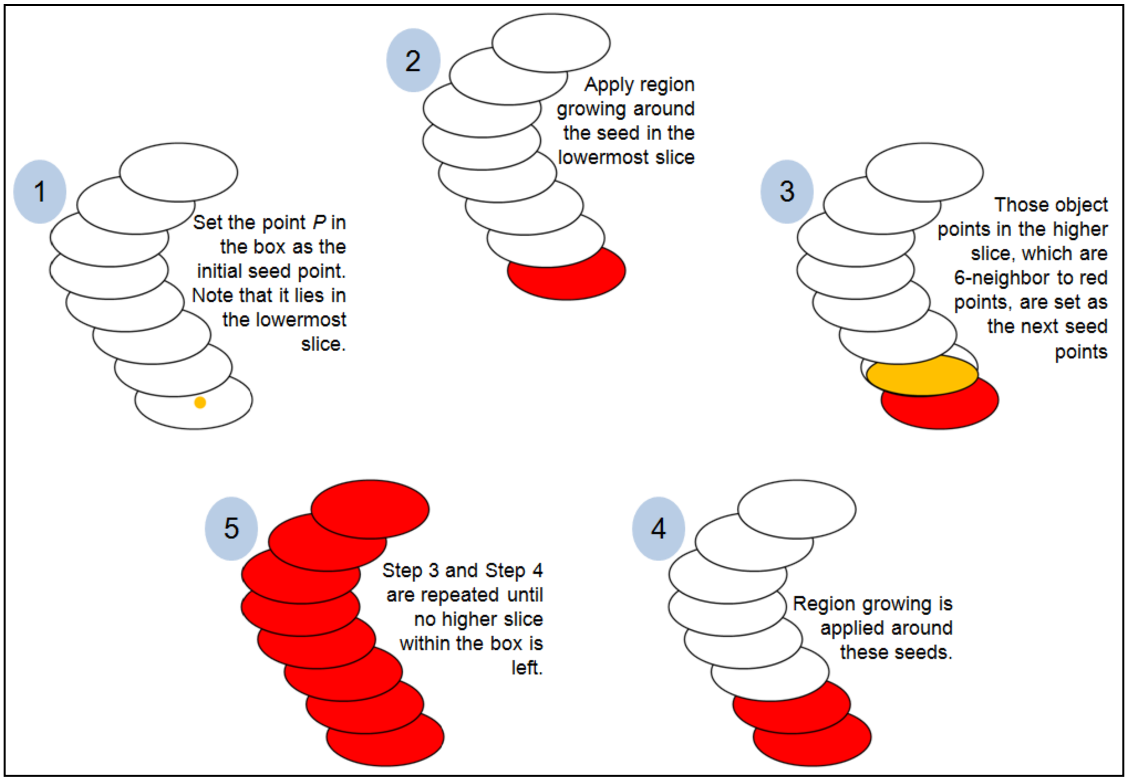

Figure 2.10 - Illustration of the entire volume growing process.

2.2.6. Setting New Initiators

Having completed the volume growing process around all points *P*, next step is determining new initiators, i.e. new starting point and direction combinations. This is necessary for automatic continuation of the following process. By automatic determination of new initiators, no further user interaction is required.

To achieve automatic determination of new starters, a cube is created around previously found junctions, which are on the tracked branch. This cubic volume of interest has dimensions $H_0 \times H_0 \times H_0$. Apparently, there can be some branches included in the cube, which are not connected to the junction. A 24-connectivity checking process is implemented within the cube to distinguish between branches which are connected to the junction and foreign branches. Branch portions, which are not 24-connected to the junctions are suppressed.

Keeping the definition of a junction in mind, there exists at least three intersection points on the surface of the cube, where skeletons of the connected branches and the cube surfaces meet each other. Vectors pointing from the junction at the intersections are calculated. These vectors are potentially the next starting directions, where the junction is assumed to be the next starting point. Note that two of these intersections are previously tracked, they are now ignored to avoid double tracking. Remaining intersections are set to be the next starting directions. The process on setting new initiators is illustrated in Figure 2.11.

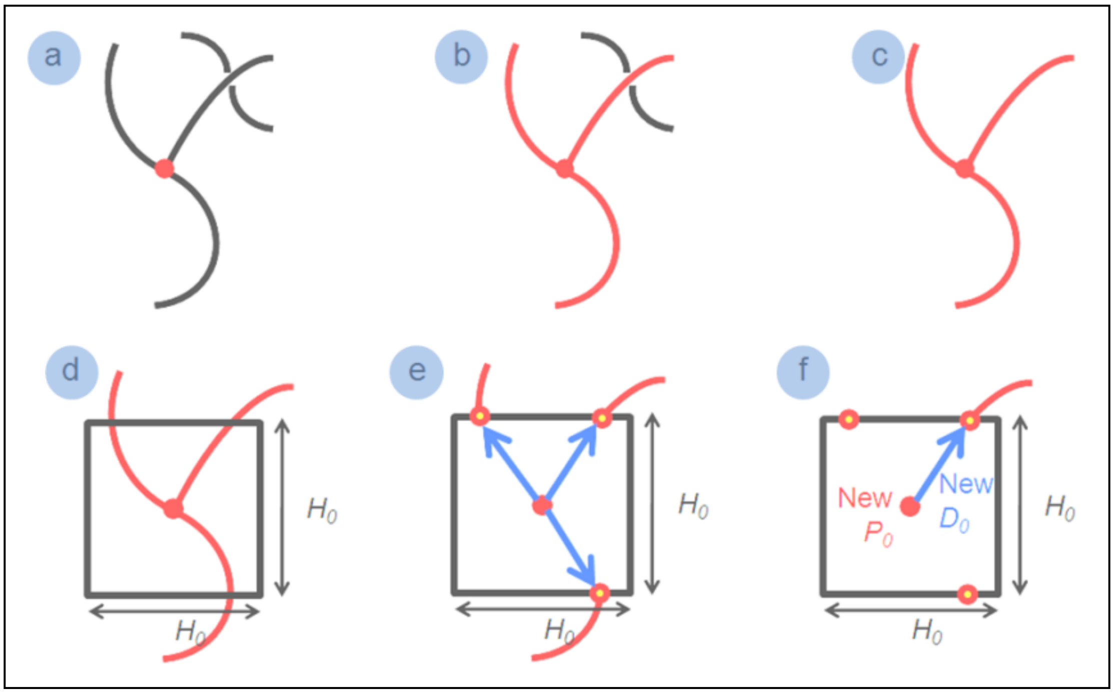

Figure 2.11 - Illustration on setting the new initiators. a) A cubic volume is created around the distinguished junction. b) Branches, 26-connected to the junction, are determined. c) Foreign branches are removed. d) Intersections of branches' skeleton with the cube surfaces are searched. e) Vectors through the junction and the intersection points are calculated. f) Previously tracked intersections are ignored. The remaining vectors are set to be the next starting directions, where the next starting point is set as the junction.

CHAPTER 3

RESULTS AND DISCUSSION

3.1. Single Branch Tracking

Main parameters acting on the performance of single branch tracking are the dimensions of local box in which gravity center is computed, directional constant k_d, spatial replacement constant k_p, and lower limit of total intensity values in the local box. As well as other results in this chapter, the affects of all these parameters are observed on 3-D angiographic image data of real patients.

Box dimensions assertively affect the tracking capability by determining the local volume of interest. Larger dimensions let foreign branches go into the local volume and slide the gravity center to outside of the branch under consideration. This situation may lead to false tracking so that the local box may skip from the user-defined branch to a neighboring branch at an irrelevant position. Therefore, large dimensions of local box can mislead the process to a network which is not directly connected to user-defined starting point, while box dimensions large enough to cover the lumen of vessels lead to the right path. Figure 3.1 depicts two different results of tracking procedure on the same volume. In the first procedure, box base has twice larger dimensions and box skips to neighboring branch since gravity center does so. In the second procedure, box base dimensions slightly cover lumen, hence remains within the right track.

Height of the box, on the other hand, has a different effect on catching discontinuities of vessel lumen. That is, depending on the box height, one can track branches even if they have their portions disconnected due to low contrast ratio. Figure 3.2 illustrates a branch with disconnected portions is tracked by the algorithm.

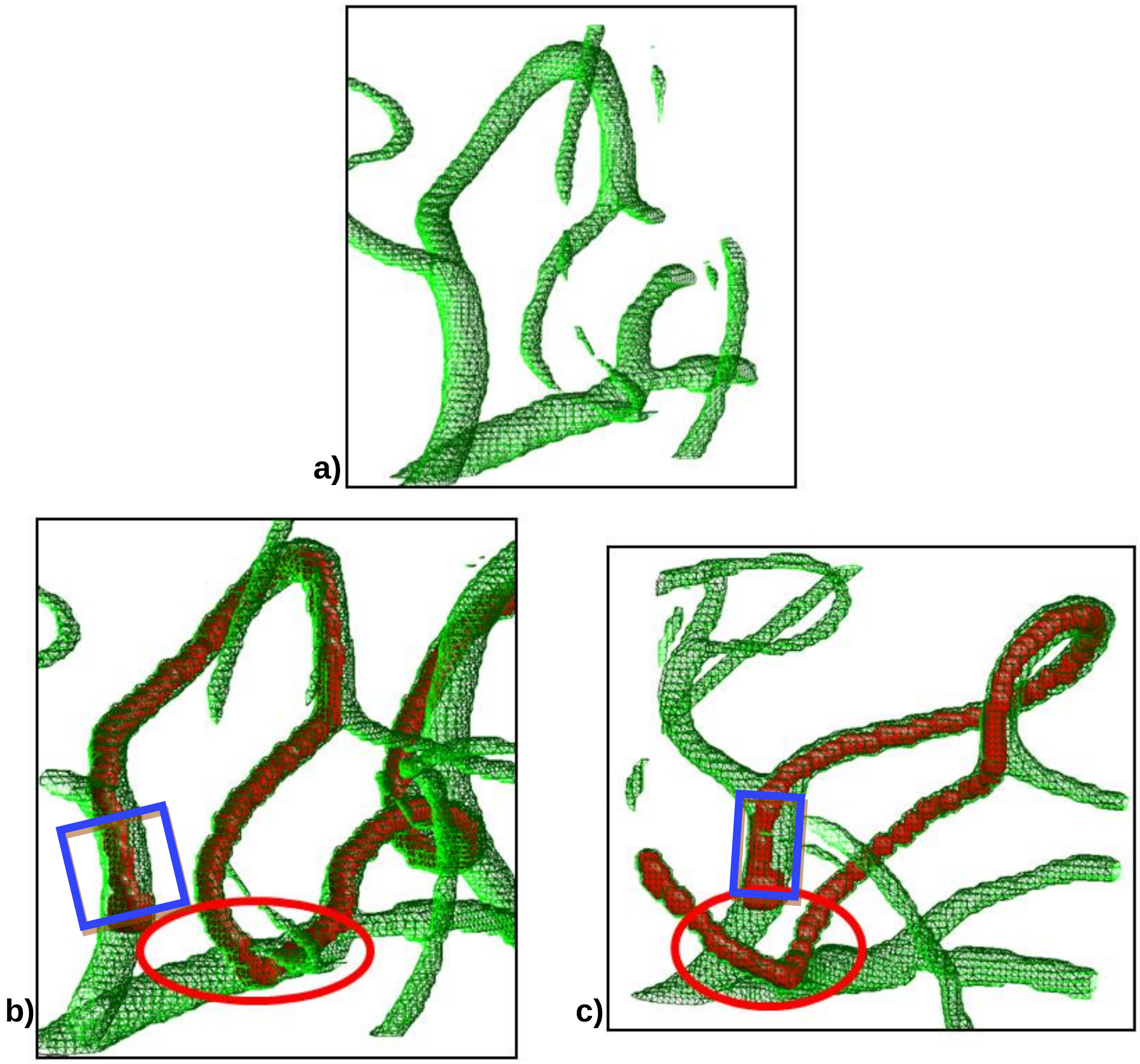

Figure 3.1 - Effect of box dimensions on tracking performance. a) Volume of interest. b) Tracking fails when box dimensions are twice larger than vessel lumen width. The blue rectangle represents the box located at the user-defined starting point in the user-defined starting direction. c) Box dimensions enough to cover the lumen achieves tracking the right track. The blue rectangle represents

the box located at the user-defined starting point in the user-defined starting direction.

a)

b)

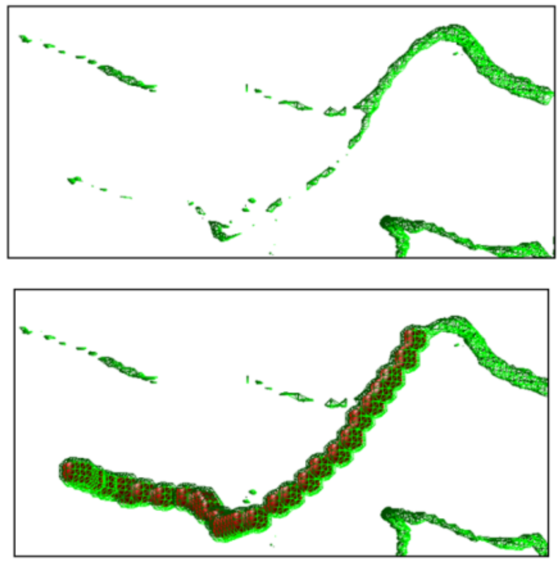

Figure 3.2 - Longer boxes can track the branches with disconnected portions. a) A branch with disconnected branches. b) Tracking procedure could cover it.

As discussed in Section 2.2.1, k_d establishes a historical linkage between two successive gravity centers. Numerical value assigned to k_d during computations determines the dependency of next tracking direction on the former direction. As k_d increases, this dependency vanishes, while $k_d = 0$ sets all tracking directions to initial user-defined direction. For the case $k_d = 0$, the algorithm cannot cover curvy branches (Figure 3.3); it cannot proceed further than the extrema of a curvature. For this reason, tracking curvy branches of cerebral vessel trees require a nonzero $\boldsymbol{k_d}$. On the other hand, any nonzero $\boldsymbol{k_d}$ yields complete coverage of curvatures (Figure 3.4).

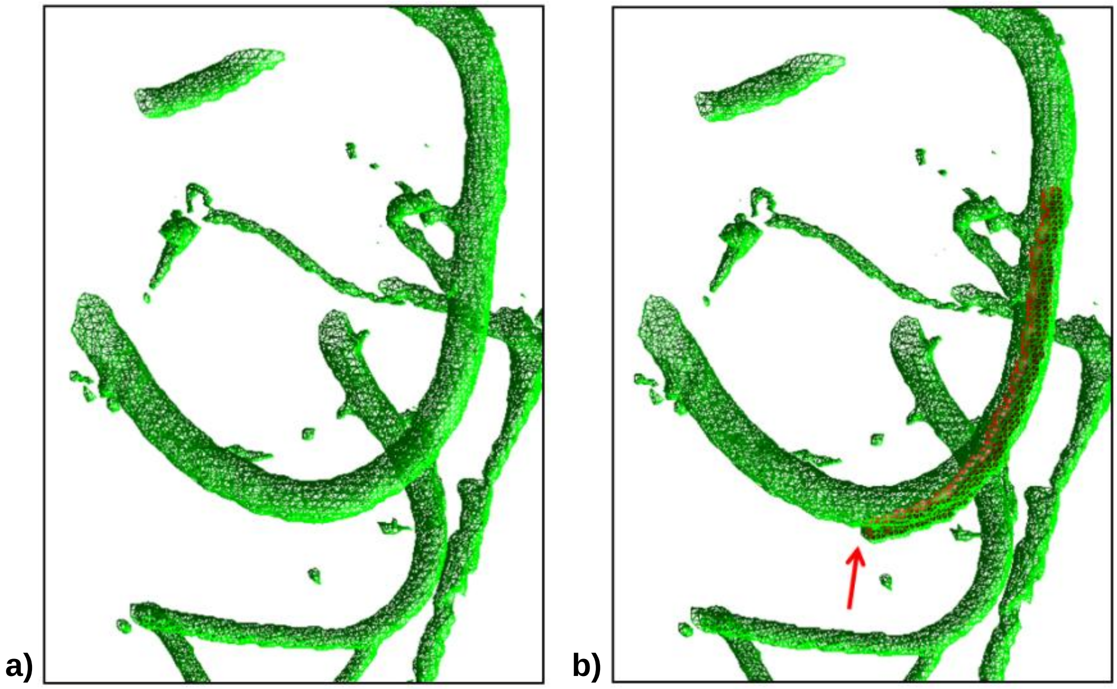

Figure 3.3 - kd affects algorithm's ability to track curvatures. a) A curvy branch. b) k_d = 0 cannot proceed further through a curve.

a)

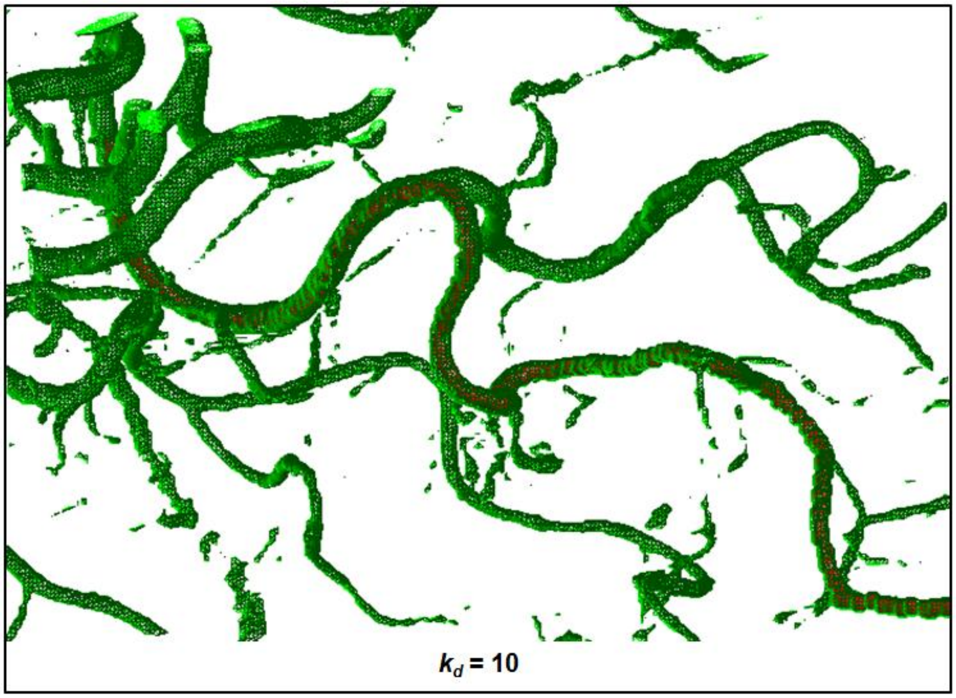

b)

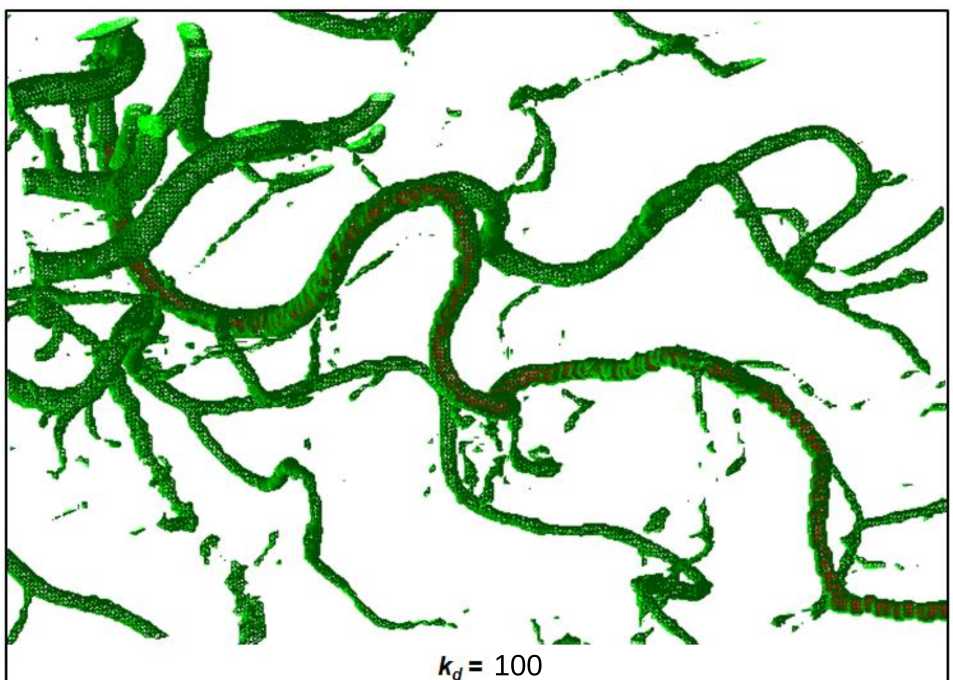

Figure 3.4 - Any nonzero k_d achieves good performance to track curvatures. a) k_d = 10. b) k_d = 100. c) k_d = 3000.

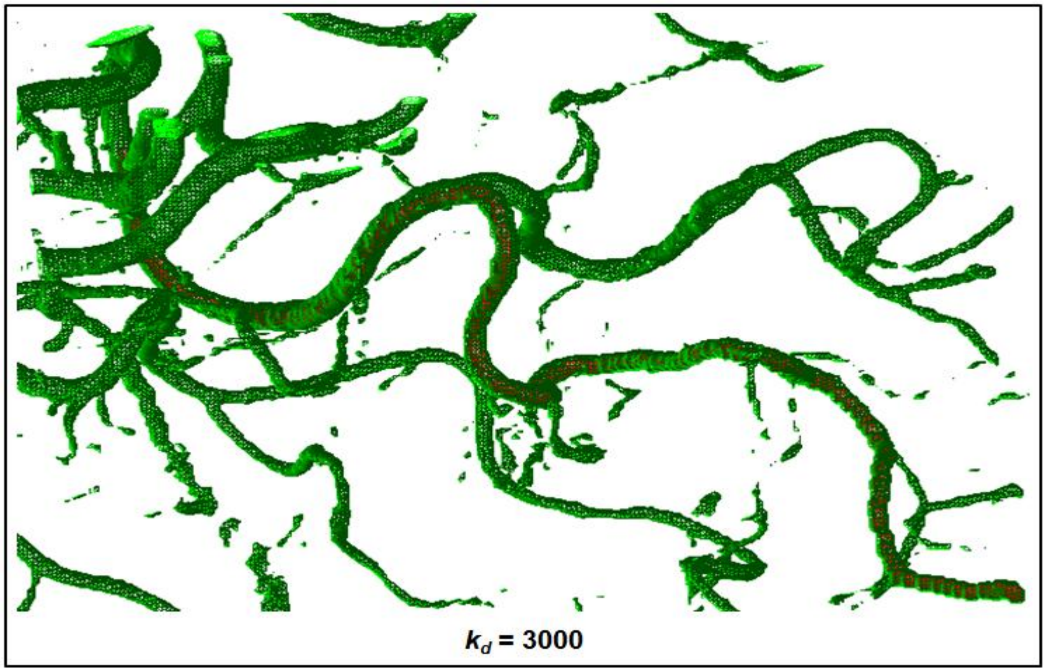

c)

Figure 3.4 - Any nonzero k_d achieves good performance to track curvatures. a) k_d = 10. b) k_d = 100. c) k_d = 3000 (continued).

Spatial replacement constant $\boldsymbol{k_p}$ determines how close that two succeeding gravity centers should be and acts on the speed of tracking process. Lower $\boldsymbol{k_p}$ values decrease deliberateness and track a branch in less iterations, while larger values proceed deliberately and need more iterations to cover the same length of branch portion (Figure 3.5) Note that, as discussed in Section 2.2.1, the next point $\boldsymbol{P_{i+1}}$ is position somewhere in between the current point $\boldsymbol{P_i}$ and the current gravity center $\boldsymbol{B_i}$. Therefore, $\boldsymbol{P_{i+1}}$ cannot go beyond $\boldsymbol{B_i}$ for any value of $\boldsymbol{k_p}$.

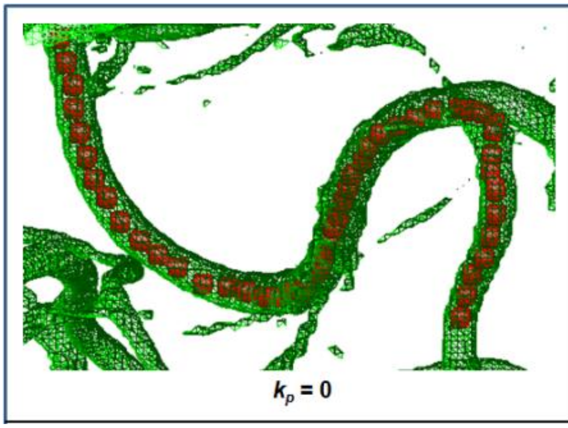

a)

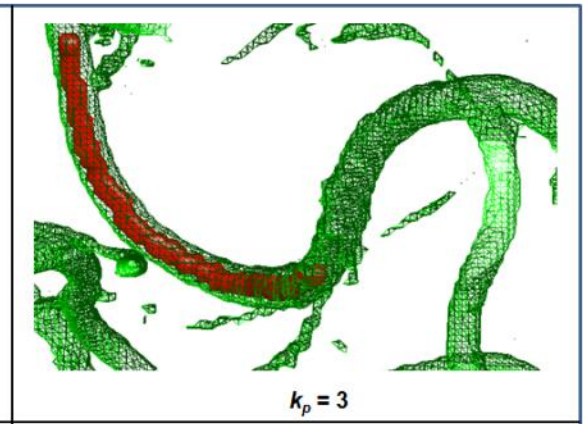

b)

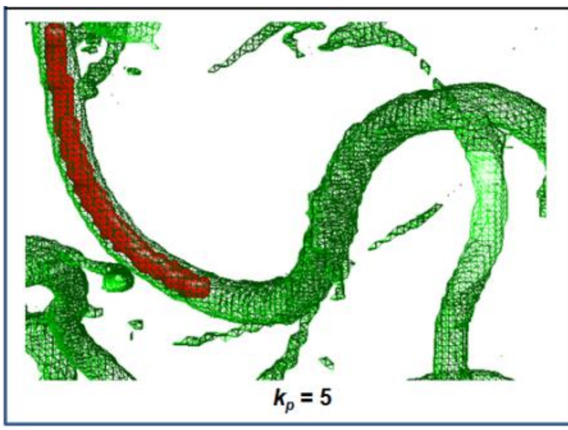

c)

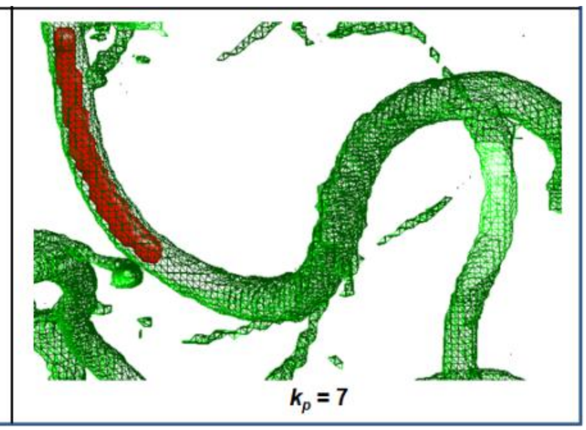

d)

Figure 3.5 - k_p affects the tracking procedure's speed and deliberateness. a) k_p = 0. b) k_p = 3. c) k_p = 5. d) k_p = 7.

In Section 2.2.1, it is stated that the summation of voxels' intensity in the local box, $\sum_{X_{\alpha,\beta,\gamma} \in V} A_{\alpha,\beta,\gamma}$, is the key parameter to terminate tracking a single branch. The process is terminated when the voxels' intensities sum up to a value, which is less than a user-defined threshold. Keeping in mind that distal voxels have small intensities, $\sum_{X_{\alpha,\beta,\gamma} \in V} A_{\alpha,\beta,\gamma}$ is lower in distal and higher in proximal portions of vessels. Then, lower threshold setting is required to reach more distal portions of branches, while higher threshold setting terminates the tracking process before reaching at distal portions.

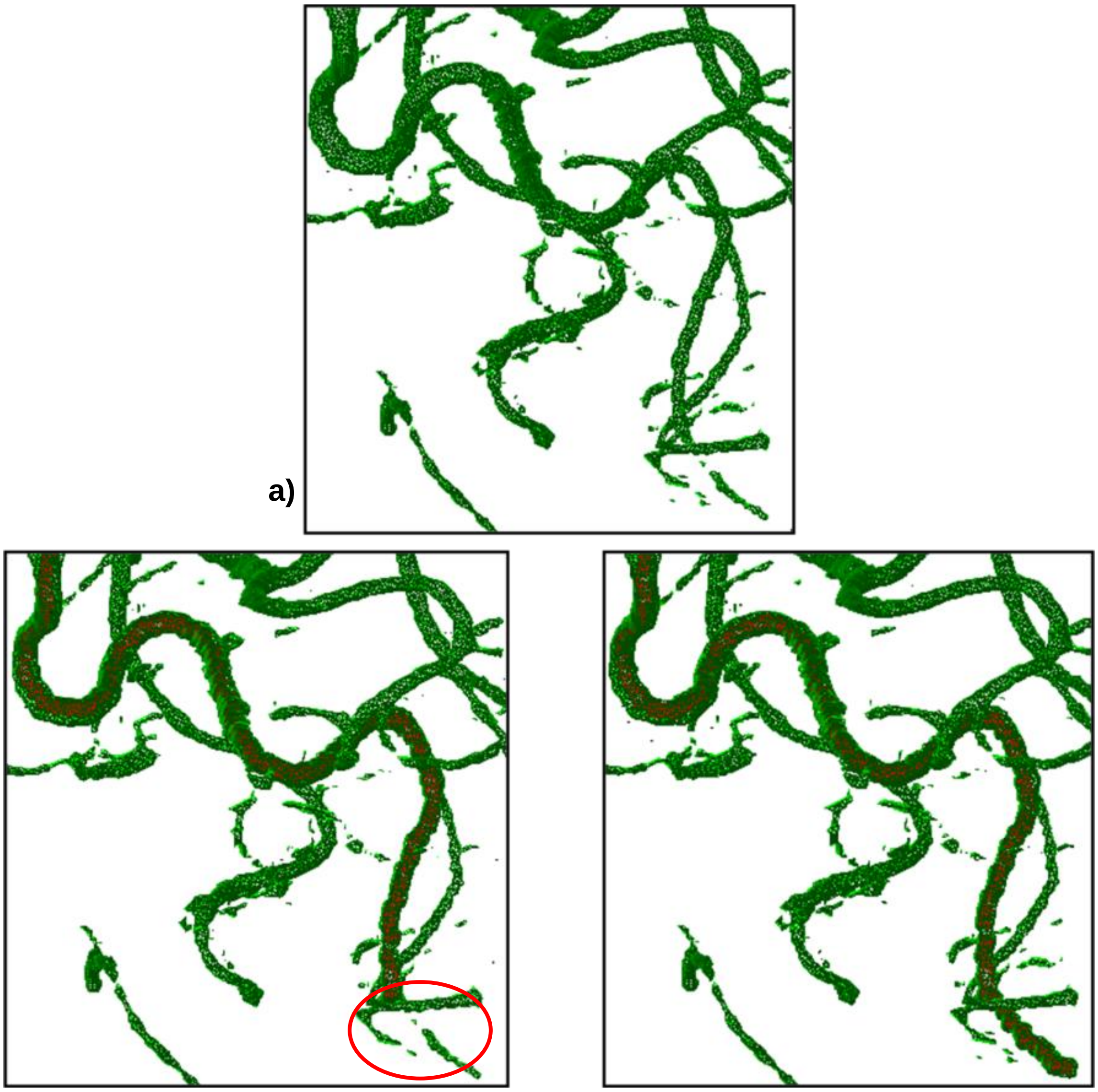

a) b)

Figure 3.6 - The limit on the summation of voxels' intensities in a local box affect the capability to cover distal branches. a) An image containing distal branches. b) Limit is set to 10000, distal portion of the branch is not tracked. c) Limit is set to 5000, distal portion of the branch is tracked.

3.2. Skeletonization

An integrated implementation of methods, as described in Section 2.2.2, presented by Palagyi et al. [**37**] and Lee, Kashyap, and Chu [**4**] resulted with true skeletonization of 3-D cerebral vessels. The algorithm achieved extracted skeletons of vascular structures both at proximal and distal portions. Figure 3.7 and Figure 3.8 show proximal and distal vessel portions, respectively, and provide the corresponding skeletons after implementation of the algorithm on them.

The simple method of pruning, discussed in Section 2.2.3, is applied on skeletons so that twigs shorter than the height of local box, are removed. This procedure achieved purification of skeleton from useless portions, while keeping meaningful junctions and connectivity. While the effect of pruning on junction detection is discussed in Section 3.3, Figure 3.9 visualizes the effect of pruning on skeletons.

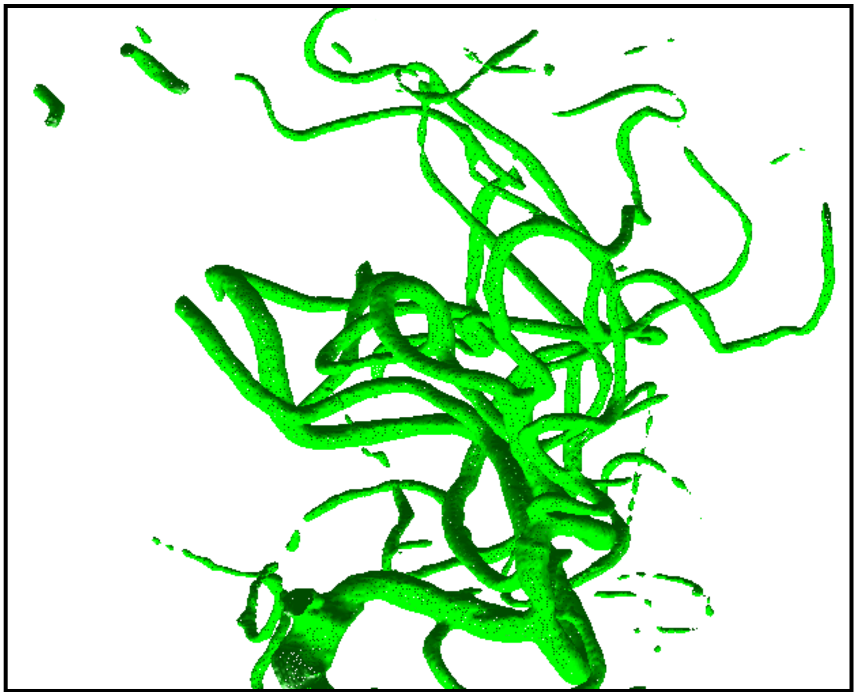

a)

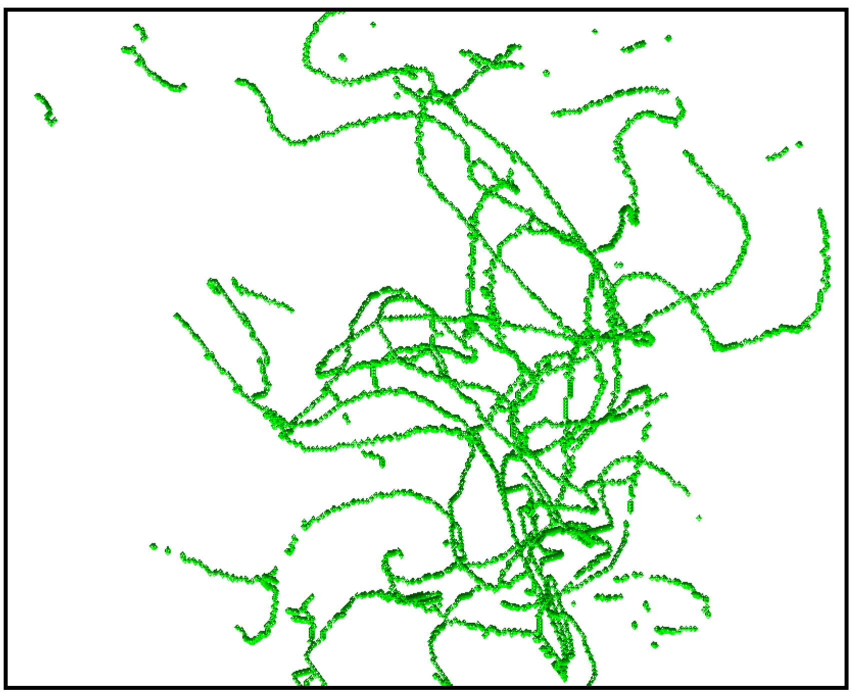

b)

Figure 3.7 - a) Proximal vessels. b) Their skeleton.

a)

b)

Figure 3.8 - a) Distal vessels. b) Their skeleton.

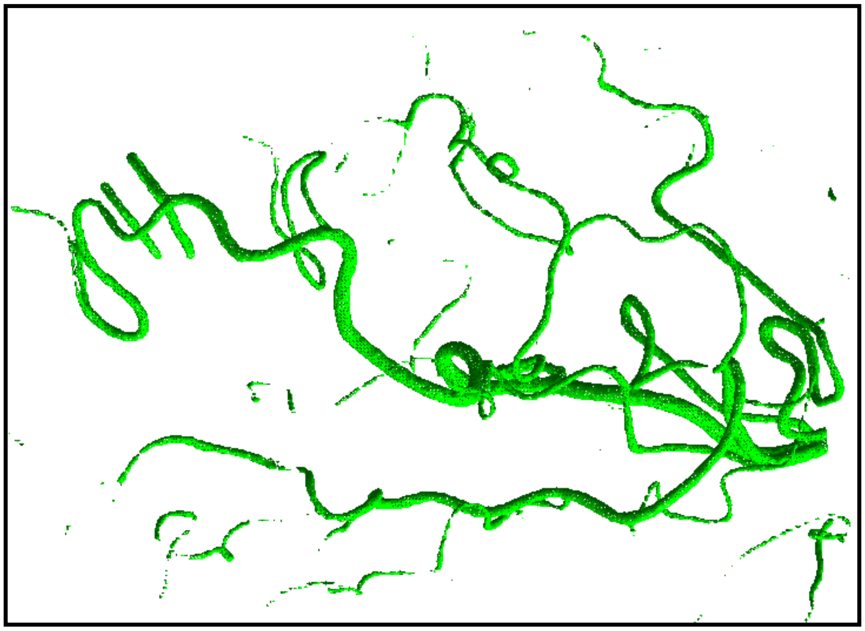

a)

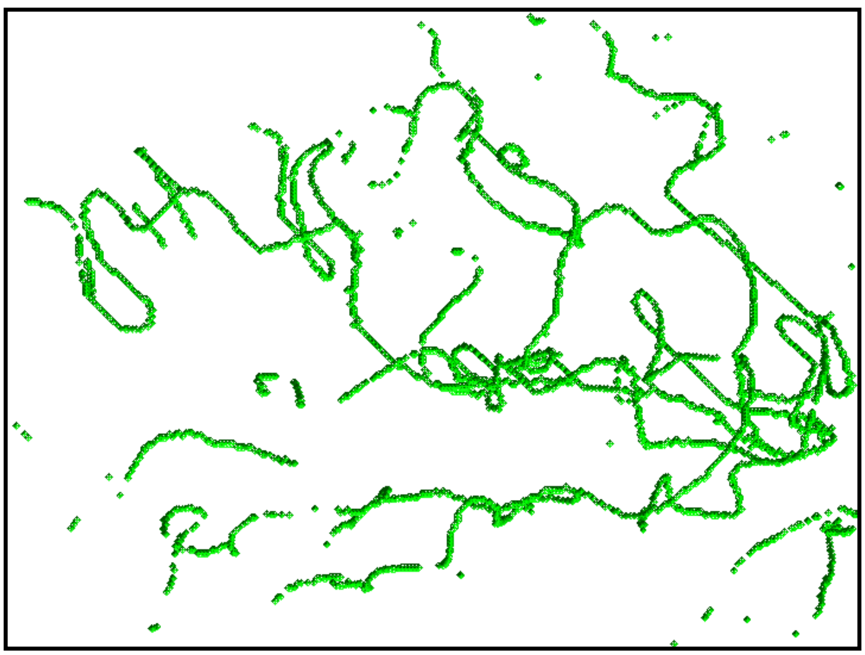

b)

Figure 3.9 - a) The volume of interest. b) Skeleton of the vessels in the volume. c) Skeleton after pruning operation. d) Voxels, which are removed during pruning.

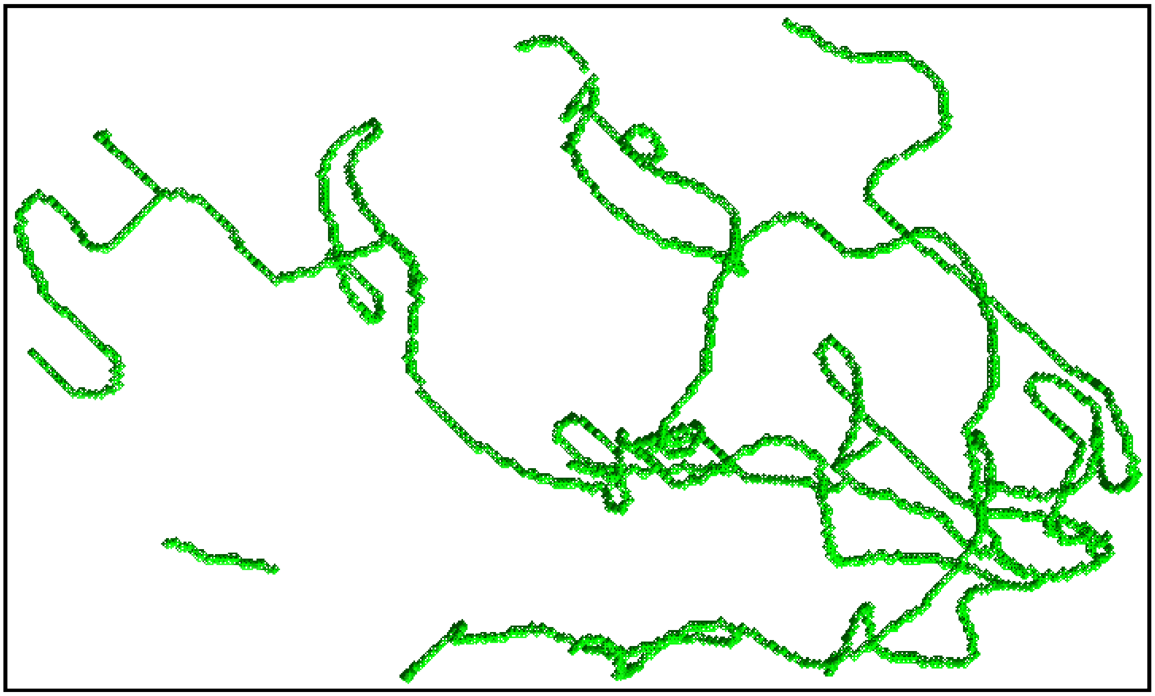

c)

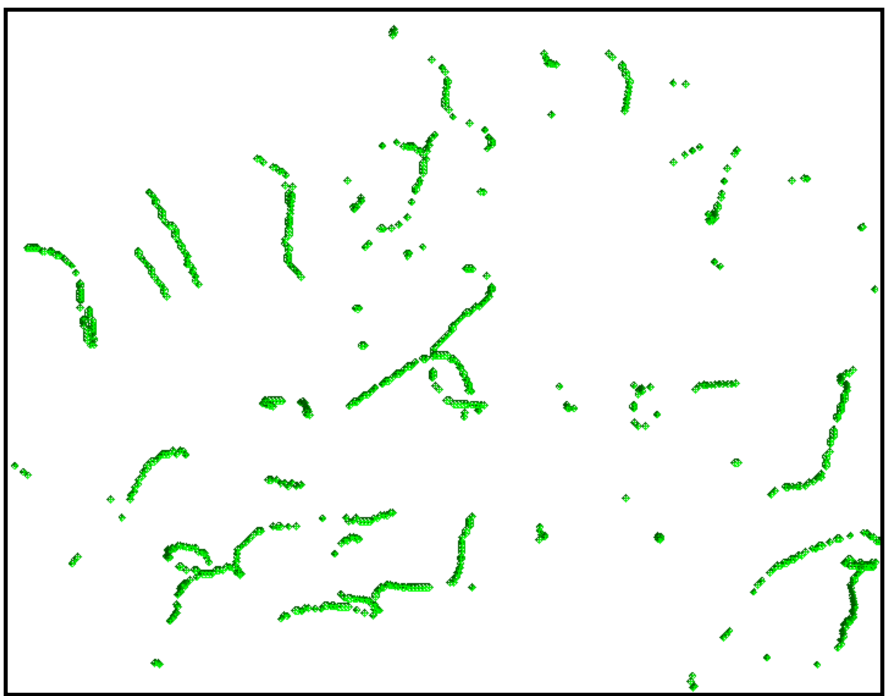

d)

Figure 3.9 - a) The volume of interest. b) Skeleton of the vessels in the volume. c) Skeleton after pruning operation. d) Voxels, which are removed during pruning (Continued).

3.3. Junction Detection

The junction detection method described in Section 2.2.4 clearly detects all the true junction within a volume of interest in a 3-D angiographic image. However, there are also false junctions detected.

False junctions originating from skeleton twigs are eliminated by applying a pruning operation on the extracted skeleton. Figure 3.10 demonstrates the effect of pruning operation, during which most false junctions are eliminated and true junctions stay. Those false junctions do not mislead to any complication in terms of tracking since they point at the same branch of interest; eliminating false junctions originating from skeleton twigs is helpful in terms of reducing the overall duration of 3-D vessel connectivity tracking operation.

On the other hand, junctions originating from superposition of some branches cannot be eliminated by pruning operation. Complication occurs since these type of junctions point at a neighboring branch, 3-D vessel connectivity tracking operation is misled at these junctions. Figure 3.11 demonstrates that a local thresholding method can help discriminating two superposed branches and eliminating this type of false junctions.

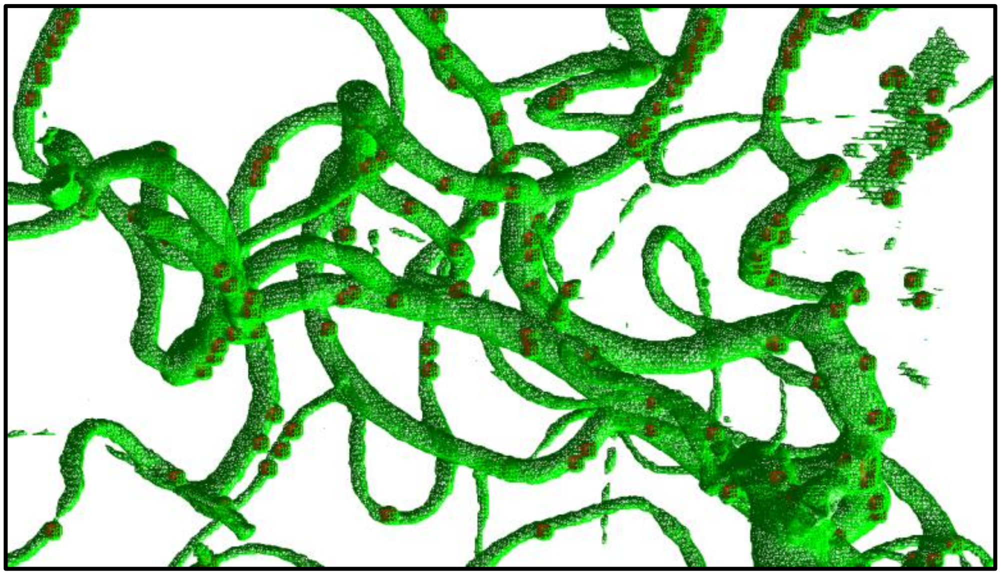

a)

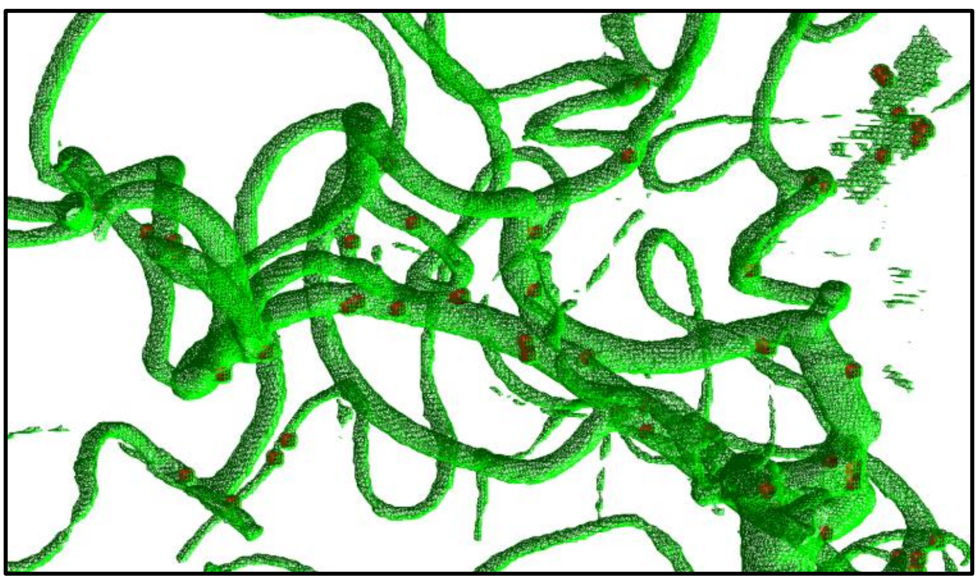

b)

Figure 3.10 - a) Red dots mark the junctions before pruning operation. b) Red dots mark the junctions after pruning operation. Pruning operation reduced the number of junctions from 244 to 76.

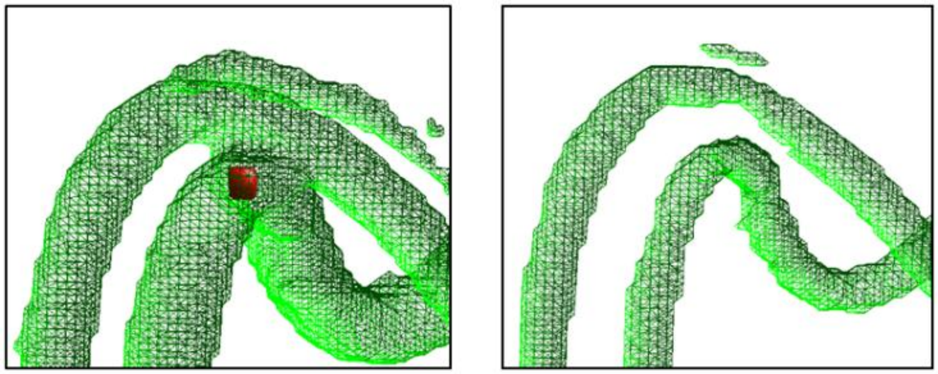

a) **b)**

Figure 3.11 - a) Two superposed branches, yielding a false junction. b) The superposed branches are discriminated by a local thresholding procedure, the false junction is removed.

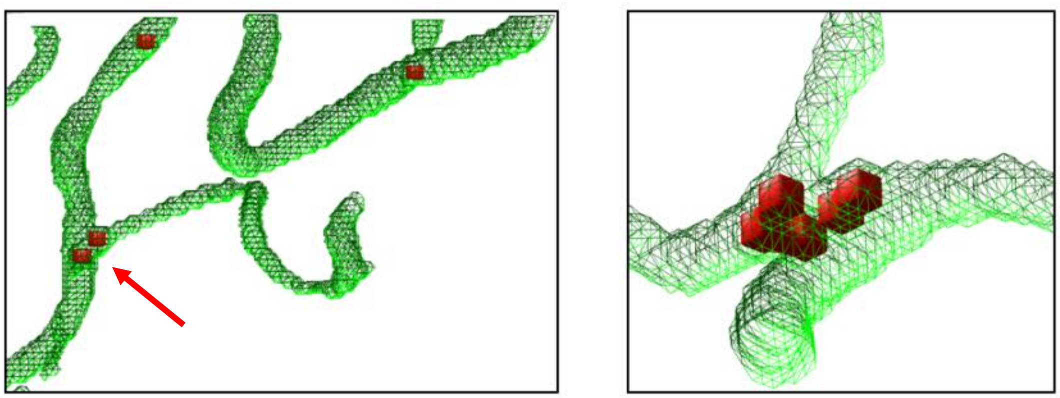

a) **b)**

Figure 3.12 - A closer look at detected junctions. a) Red dots showing the junctions. One of the junctions pointed by the arrow is due to a skeleton twig. b) Junctions marked by red dots are due to superpositioning of branches.

3.4. Distinguishing Junctions on the Tracked Branch

Following the junction detection operation, all the junctions within the volume of interest are revealed. However, only those junctions, which are on the tracked branch are useful, the rest must be eliminated since they lead to complication in the tracking process.

Volume growing method is applied, as discussed in Section 2.2.5, around points P_i as a distinguishing tool: Only the junctions located in this grown volume are considered to keep 3-D vessel connectivity tracking operation continuing. These contained junctions are the points, where new connected single branches arise. Therefore, next single branch tracking procedures are initiated from these junctions. On the other hand, the junctions outside the grown volume are removed since they make no contribution on tracking the next connected individual branches.

3.5. Setting New Tracking Initiators

Tracking of a single branch is completed by computing new directions on distinguished junctions to start next tracking procedure. Setting a junction on the tracked branch as the new P_0, and assigning the corresponding direction as the new D_0, tracking procedure for the next connected and distal branch can be initiated.

Assignment of new initiators P_0 having initial direction D_0 is depicted in Figure 3.19, based on the junctions contained in the grown volume and orientations of distal branches going out of those junctions.

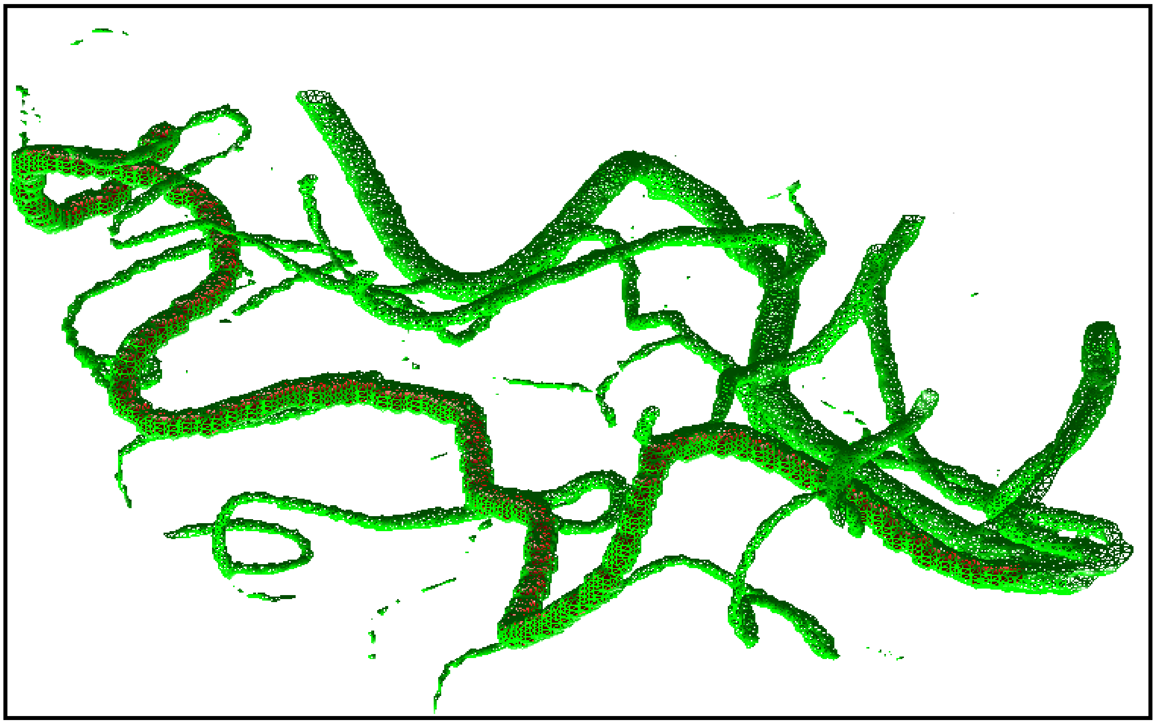

Figure 3.13 - A vascular network, in which the red branch is tracked.

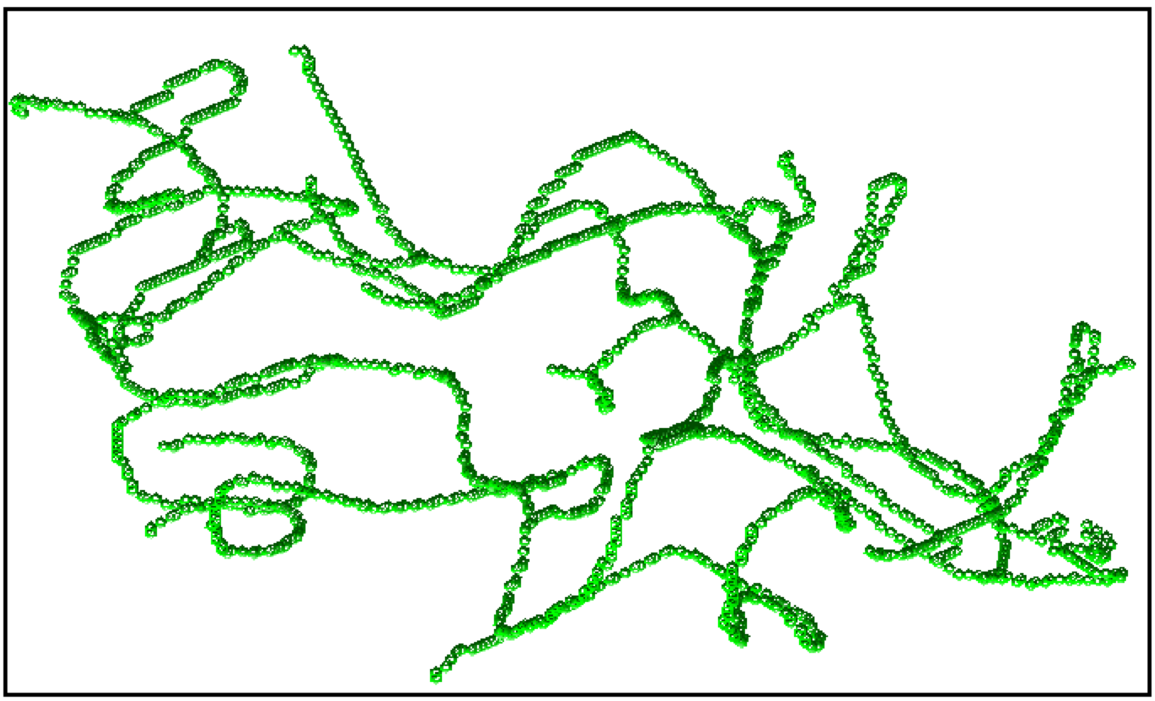

Figure 3.14 - Pruned skeleton of the volume of interest.

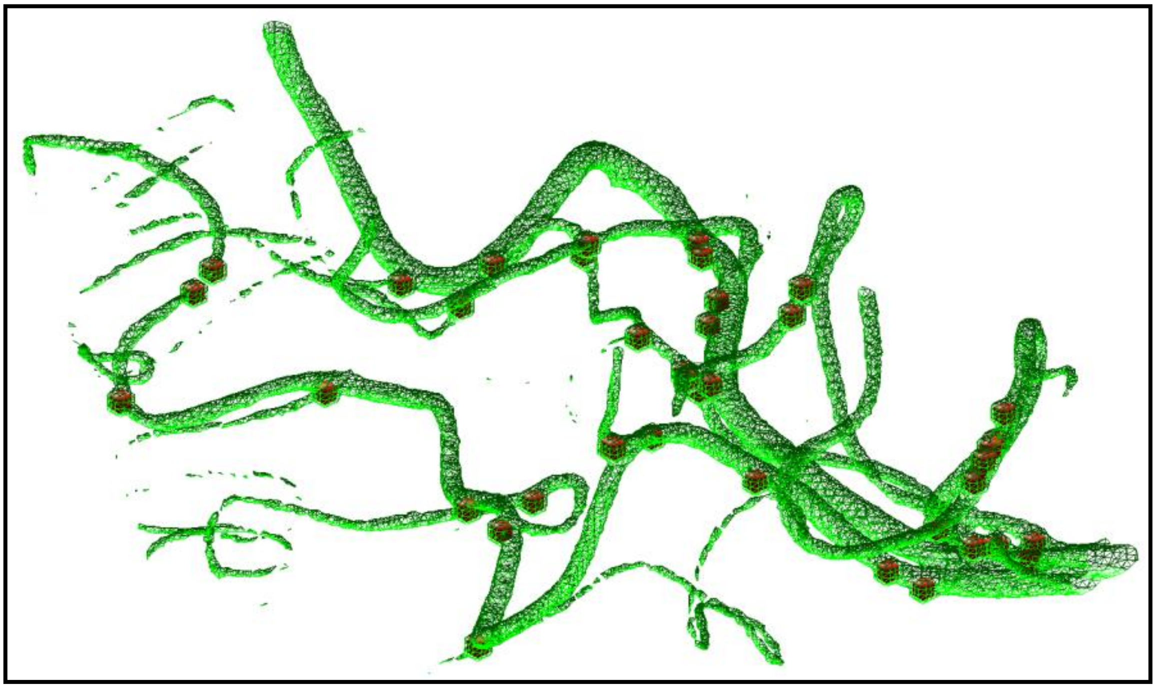

Figure 3.15 - All junctions within the volume of interest.

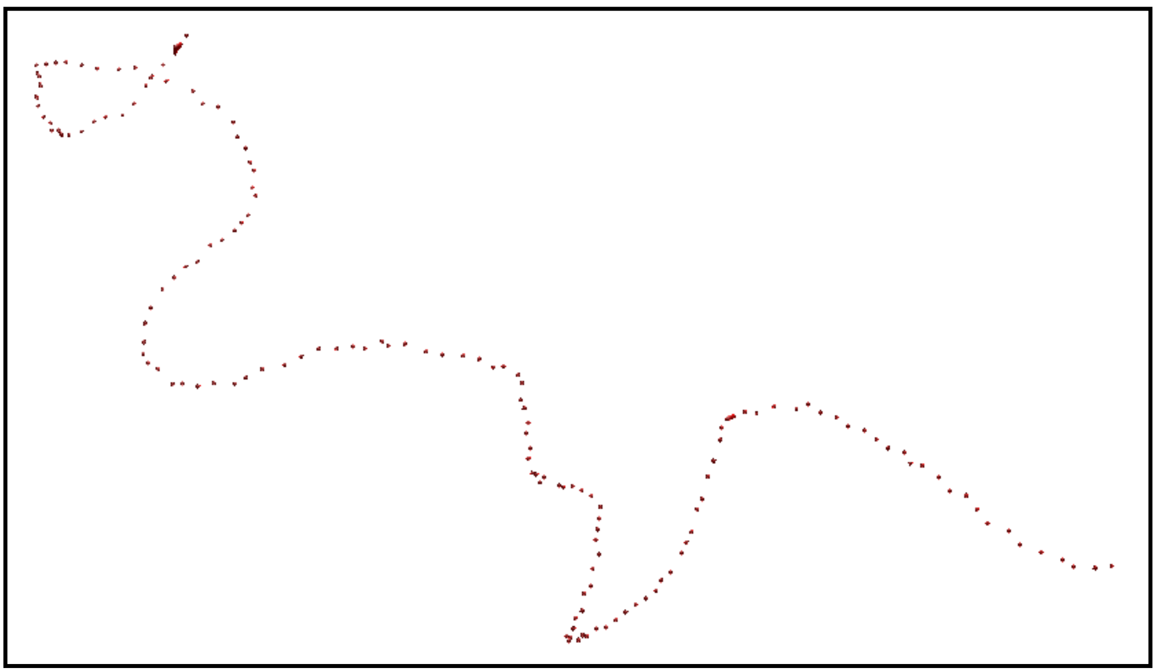

Figure 3.16 - The points Pi of the tracked branch.

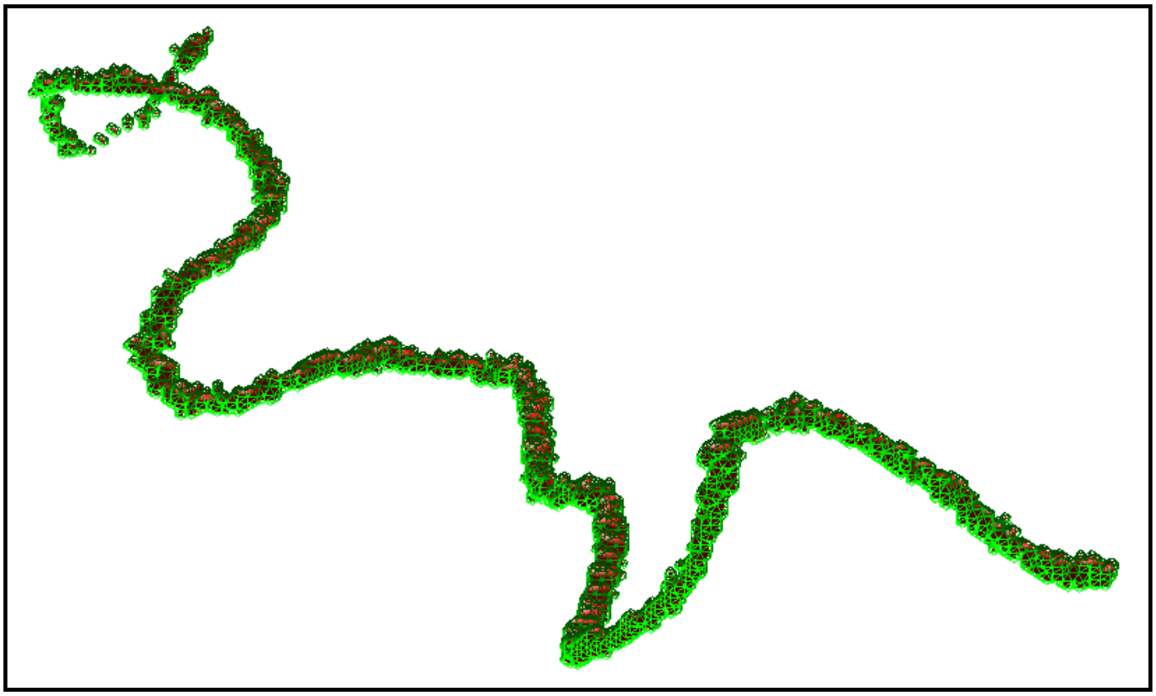

Figure 3.17 - The recovered branch, recovery is achieved by volume growing around the seed points Pi.

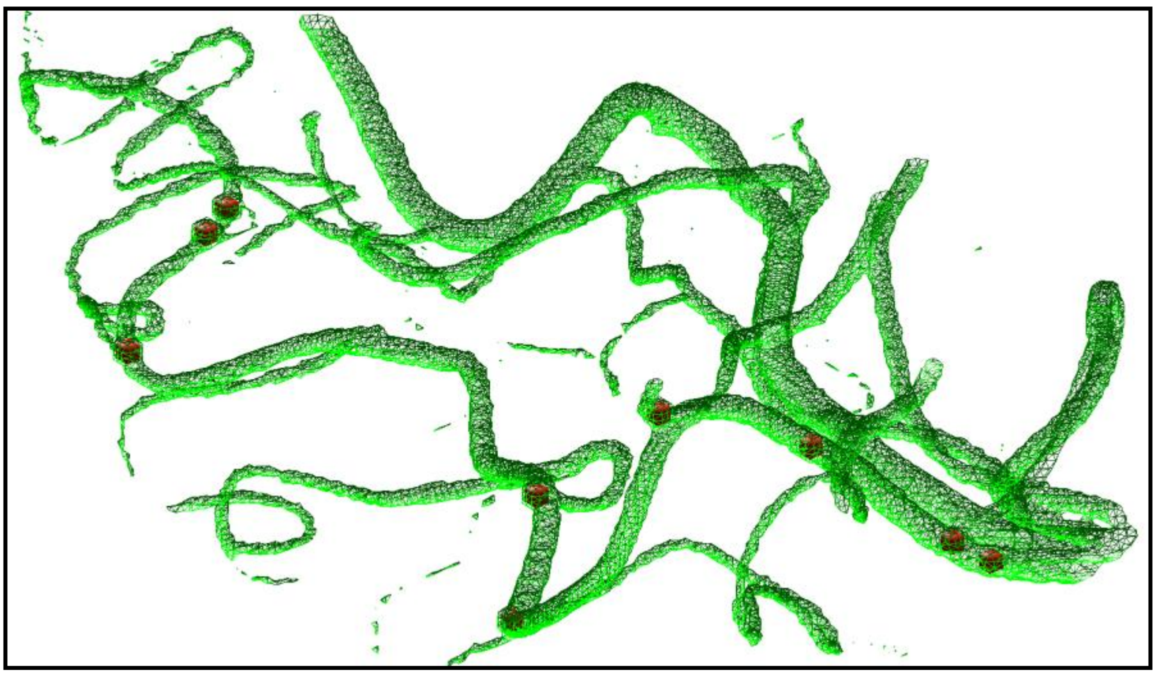

Figure 3.18 - Distinguished junctions, located in the grown volume.

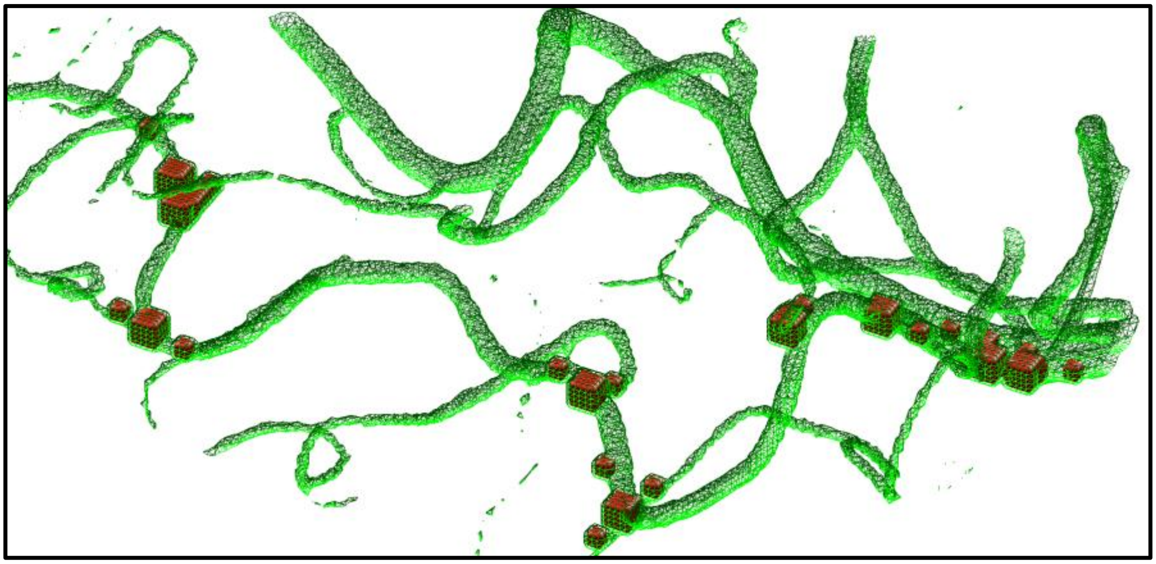

Figure 3.19 - The new starting points (big red dots) and corresponding directions (small red dots) Note that superposed neighboring branches are also to be tracked.

CHAPTER 4

PERFORMANCE EVALUATION

Performance of the algorithm is evaluated on a basis of visual inspection. Real patient image data are used as well as image data of a visually complex physical phantom.

4.1. Evaluation Methods

4.1.1. Performance Evaluation on Real Patient Image Data

The algorithm has been implemented on images from 4 patients, where 2 starting point and direction combinations are selected by an expert interventional radiologist to be clinically meaningful. A sample patient image and starting combination is depicted in Figure 4.1.

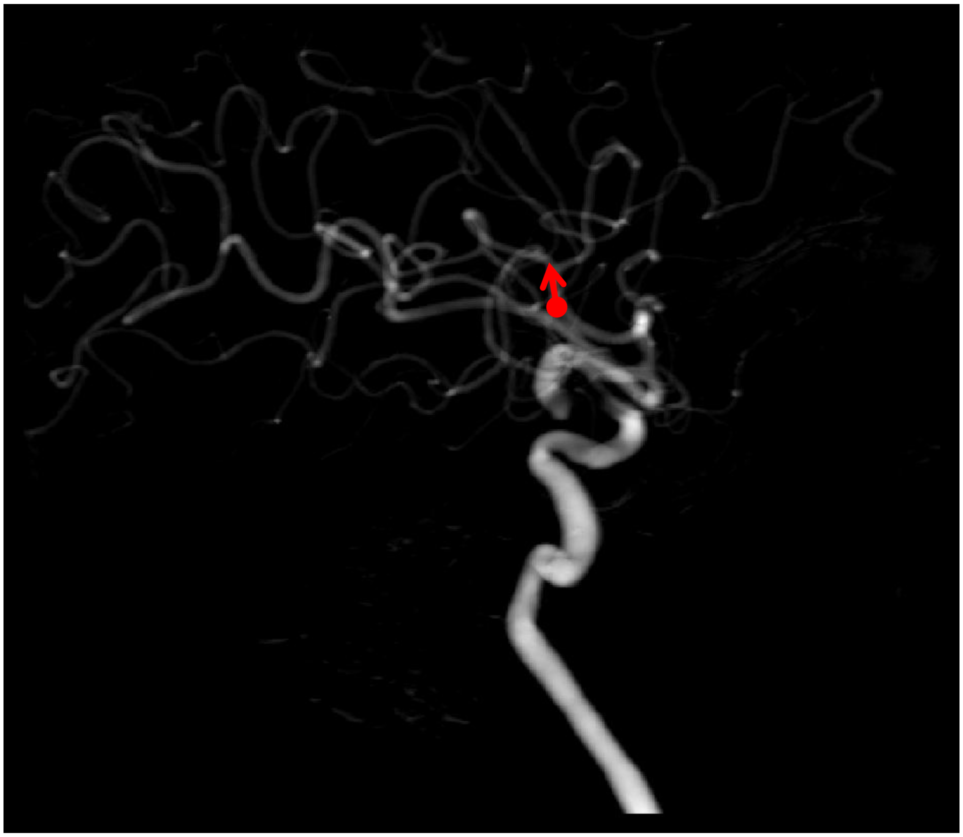

Figure 4.1 - A sample patient image depicting the starting point and direction as defined by an expert interventional radiologist.

Starting from those points in the specified directions, algorithm has extracted the network connected to the points in the specified directions. The results are viewed by two radiologists, they checked the validity of the algorithm's decisions in terms of branch tracking and junction detection. They counted the true and false positives as well as the true and false negatives.

Identification of true positives, false positives, true negatives, and false negatives is as follows:

True Positive (TP): Algorithm detects a point as a junction, which is detected as a junction also by the radiologists.

False Positive (FP): Algorithm detects a point as a junction, which is not detected as a junction by the radiologists.

True Negative (TN): Algorithm states a point is not a junction, which is actually not a junction as stated also by the radiologists.

False Negative (FN): Algorithm states a point is not a junction, which is stated to be a junction by the radiologists.

Once these numbers are obtained, sensitivity, specificity, false negative rate, and false positive rate of the algorithm are calculated as suggested in [**45**][**46**]**.**

4.1.2. Performance Evaluation on Physical Phantom's Image Data

A visually complex object shown in Figure 4.2 has been constructed to evaluate the performance of the algorithm by utilizing images of the phantom and having the ground truth information.

Figure 4.2 - Physical phantom object, having two branches each with two junctions.

The phantom had two branches, each one having two junctions, that is the complete object has five junctions. The algorithm is implemented on three different branches in the object: First implementation is started at the root, and the other two combinations are started at the two branches.

After having the object constructed, its 3-D angiographic image is acquired and the algorithm is implemented on it. A 2-D fluoroscopy image of the phantom and a 2-D projection of 3-D image are shown in Figure 4.3 and Figure 4.4, respectively. Algorithm has been implemented on this post-processed image. A portion of resulting image after the implementation of the algorithm is given in Figure 4.5. Affect of branch superposition is observed on two different configurations. The true and false positives as well as the true and false negatives are counted; and than sensitivity, specificity, false negative rate, and false positive rate of the algorithm are calculated [**45**][**46**].

Equations to calculate above-mentioned metrics regarding the numbers of true positives, false positives, true negatives, and false negatives are given as:

$$Sensitivity = \frac{TP}{TP + FN} \ ,$$

$$Specificity = \frac{TN}{TN + FP} \ ,$$

$$False\ Positive\ Rate = \frac{FP}{TN + FP} \ ,$$

$$False\ Negative\ Rate = \frac{FN}{FN + TP} \ .$$

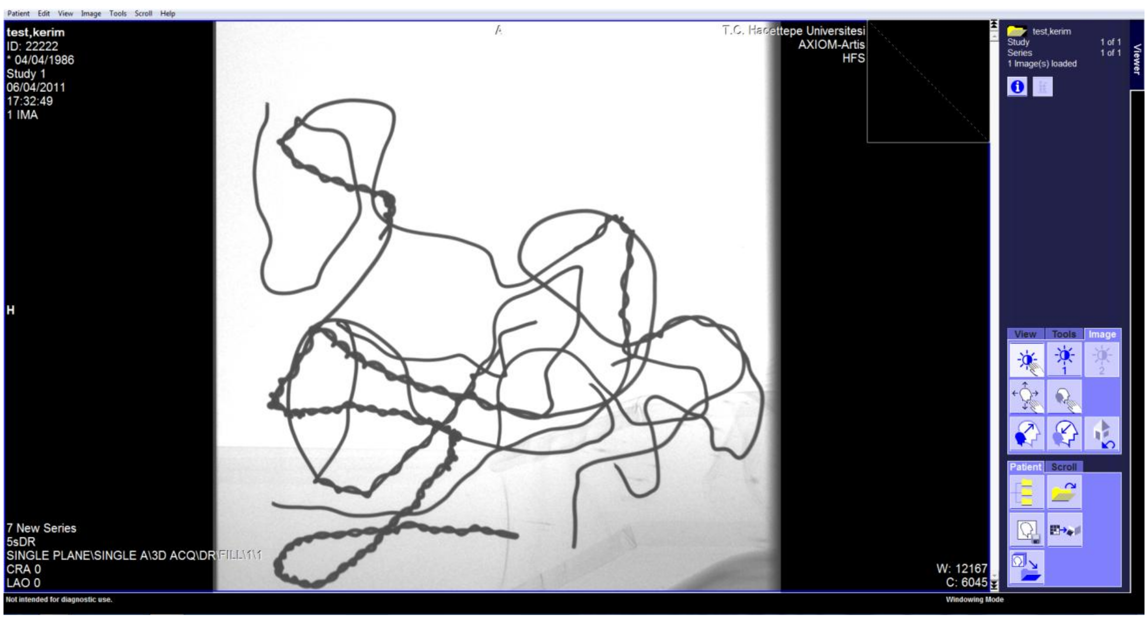

Figure 4.3 - 2-D Fluoroscopy image of the physical phantom.

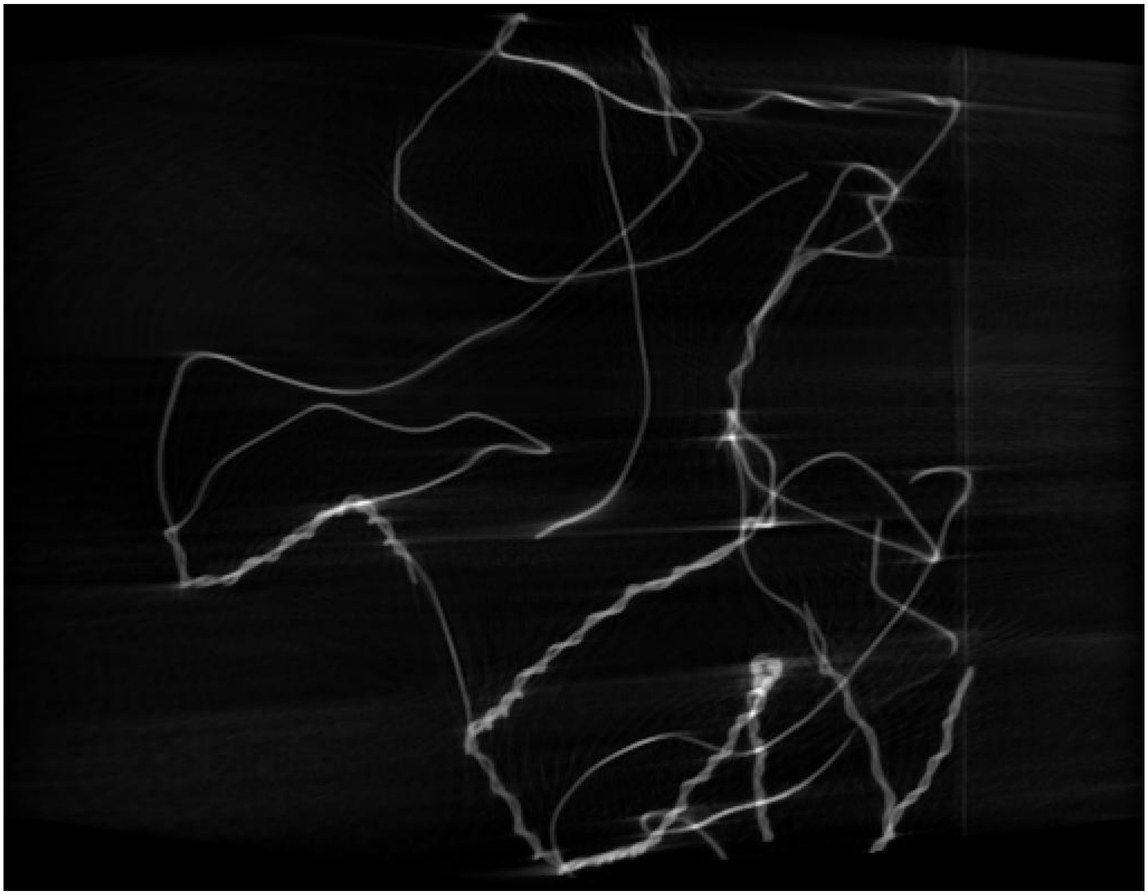

Figure 4.4 - 2-D projection image of the physical phantom's 3-D angiographic image, created via Matlab. This projection image is used as an interface to set initiators. The artifacts in the images are suppressed by simple global thresholding.

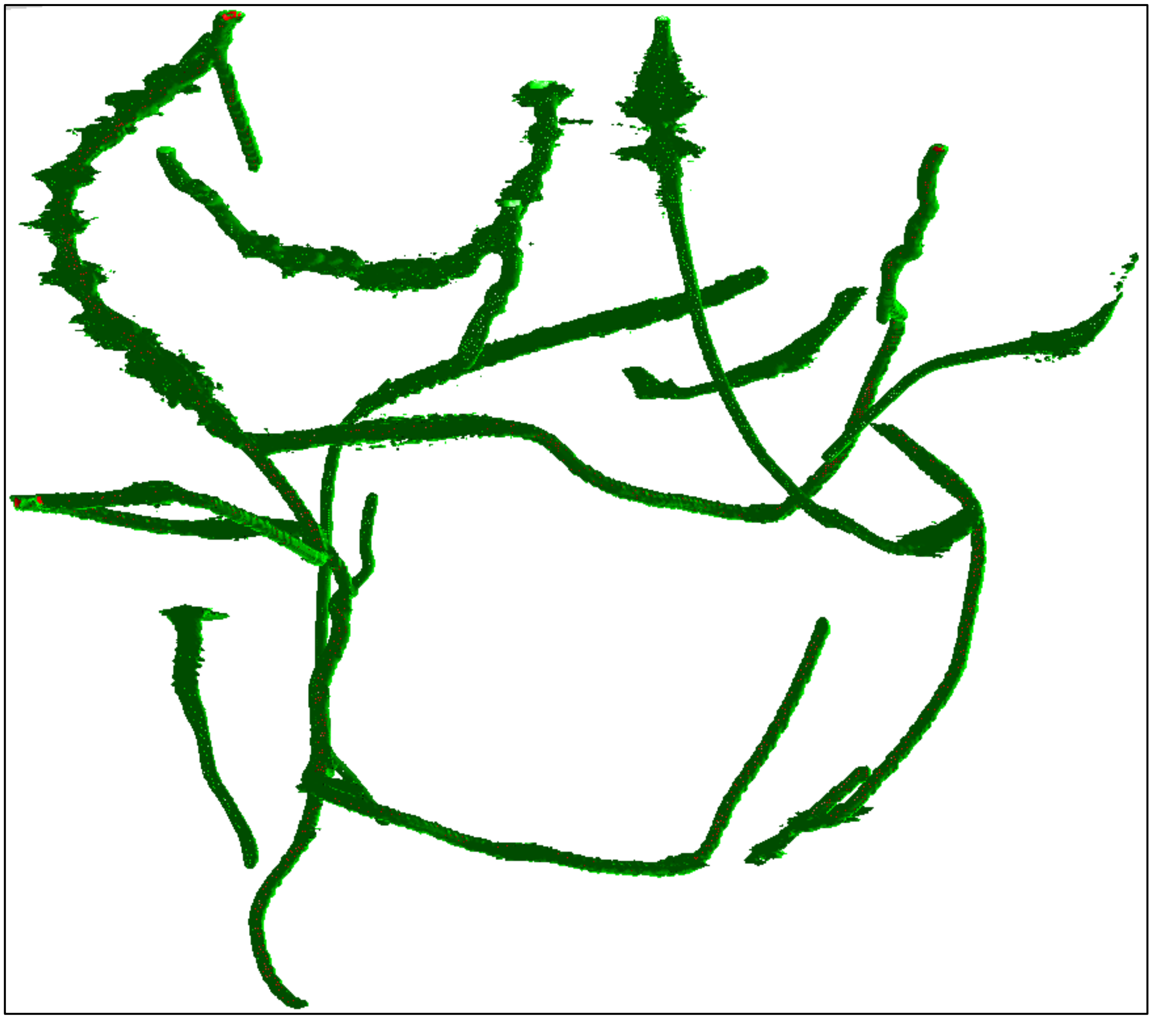

Figure 4.5 - Visualization of the physical phantom's 3-D image in Matlab. Since this 3-D image of the physical phantom includes a huge amount of data in it, entire image cannot be visualized in Matlab.

4.2. Evaluation Results

4.2.1. Performance of the Algorithm on Real Patient Image Data

The numbers of true positives, false positives, true negatives, and false negatives for each patient are given in Table 4-1 as they are counted by visual inspection.

Table 4-1 - Numbers of true positives, false positives, true negatives, and false negatives in patient data as counted by the radiologists.

	True Positives	**False Positives**	**True Negatives**	**False Negatives**
Patient A, Point 1	7	1	10709990	2
Patient A, Point 2	9	1	10449989	1
Patient B, Point 1	6	2	10229992	0
Patient B, Point 2	8	1	11029990	1
Patient C, Point 1	7	2	10539991	0
Patient C, Point 2	11	3	12099985	1
Patient D, Point 1	8	1	10609989	2
Patient D, Point 2	9	2	11649986	3

Based on the values given in Table 4-1, performance of the algorithm is evaluated on each patient's starting point and direction combination. The results are provided in Table 4-2.

Table 4-2 - Calculated values of sensitivity, specificity, false negative rate, and false positive rate corresponding to patient data.

	Sensitivity	**Specificity**	**False Negative Rate**	**False Positive Rate**
Patient A, Point 1	0,77	0,99	0,22	0,93E-7
Patient A, Point 2	0,90	0,99	0,10	0,95E-7
Patient B, Point 1	1,00	0,99	0,00	1,95E-7
Patient B, Point 2	0,88	0,99	0,11	0,90E-7
Patient C, Point 1	1,00	0,99	0,00	1,89E-7
Patient C, Point 2	0,91	0,99	0,08	2,47E-7
Patient D, Point 1	0,80	0,99	0,20	0,94E-7
Patient D, Point 2	0,75	0,99	0,25	1,71E-7

4.2.2. Performance of the Algorithm on Image Data from the Physical Phantom

In the first experiment, object is shaped in such a manner that no superposing branches existed. In this case neither false positives nor false negatives are observed. Numbers of true positives, false positives, true negatives, and false negatives are given in Table 4-3, while corresponding results on sensitivity, specificity, false negative rate, and false positive rate are given in Table 4-4.

Table 4-3 - Numbers of true positives, false positives, true negatives, and false negatives in the synthetic object, while the object has no superposing branches.

	True Positives	False Positives	True Negatives	False Negatives
Combination 1	5	0	73102495	0
Combination 2	2	0	73102498	0
Combination 3	2	0	73102498	0

Table 4-4 - Calculated values of sensitivity, specificity, false negative rate, and false positive rate corresponding to the synthetic object with no superposing branches.

	Sensitivity	Specificity	False Negative Rate	False Positive Rate
Combination 1	1,00	1,00	0,00	0,00
Combination 2	1,00	1,00	0,00	0,00
Combination 3	1,00	1,00	0,00	0,00

In the second experiment, two distinct branches of two different branches are implicated so that superposition situation is simulated. In this case, one false positive is observed. Apparently, number of false positives is equal to the number of superpositions. Therefore, increasing the superpositions would increase the number of false positives. Numbers of true positives, false positives, true negatives, and false negatives are given in Table 4-5, while corresponding results on sensitivity, specificity, false negative rate, and false positive rate are given in Table 4-6.

Table 4-5 - Numbers of true positives, false positives, true negatives, and false negatives in the synthetic object, while the object has two superposing branches.

	True Positives	**False Positives**	**True Negatives**	**False Negatives**
Combination 1	5	1	74289691	0
Combination 2	2	1	74289694	0
Combination 3	2	1	74289694	0

Table 4-6 - Calculated values of sensitivity, specificity, false negative rate, and false positive rate corresponding to the synthetic object with two superposing branches.

	Sensitivity	**Specificity**	**False Negative Rate**	**False Positive Rate**
Combination 1	1,00	0,99	0,00	1,3461E-08
Combination 2	1,00	0,99	0,00	1,3461E-08
Combination 3	1,00	0,99	0,00	1,3461E-08

CHAPTER 5

CONCLUSION AND FUTURE WORK

5.1. Conclusion

In an angiography suite, vascular structure of a patient is examined and treated. These procedures are achieved by injecting contrast agent to patient's circulatory system, which is an invasive method. For therapeutic purposes, mostly X-ray angiography is preferred, which is also invasive. For an interventional radiologist, all software and hardware tools are appreciable, which are helpful in terms of achieving a task less invasively. These tools can be utilized during diagnosis, treatment planning, and risk assessment.

A neuro-radiologist uses visual inspection to determine the feeders of an arteriovenous malformation and the path reaching at a pathology. The same inspection applies during determination of distal branches, which are under risk of embolization and stroke. Lack of an automated tool for achieving these tasks drives the clinician consume more time on understanding the situation. Furthermore, the clinician has to inject more contrast agent and give more X-ray dose to make better decisions. Hence, this lack makes the procedure more invasive.

Within this work, we presented a basis of a software toolkit for vascular network extraction in 3-D angiographic images. It can be used for diagnosis, treatment planning, and risk assessment purposes; and provide an advantage on reducing contrast agent injection, X-ray dose, and time consumption.

A basic toolkit, which has the main technical components for 3-D vascular network extraction, is created. Perspectives on single branch tracking, 3-D skeletonization, 3-D pruning, 3-D junction detection, and volume growing for vascular network extraction are introduced. Methods for the implementation of the toolkit's mentioned components are clearly described.

Single branch tracking component can track vascular branches regardless of the branch has curvatures and discontinuities. Curvatures are handled so that any orientation they have can be tracked. The branch tracking can be achieved even if the branch has discontinuity, i.e. it has some portions disconnected. Note that the distance between two disconnected portions must be shorter than the height of the local box. This component also does not depend on lumen diameter and intensity between the branches, thus branches having large intensity difference and branches with stenoses can be successfully tracked.

Skeletonization component can extract the central lines of vascular structures, which carry vital importance for detecting junctions. Some parasitic skeleton portions reveal after skeletonization process, yielding parasitic junctions. Junction detection component detects all the true junctions, and the false junctions because of these portions and superposition. The parasitic portions are cleaned via the pruning component. Pruning procedure dramatically decreases the number of false junctions, which is an advantage to shorten the entire processing duration. However, false junctions due to the superposition of vessels are not cancelled within this thesis work and it is shown that local thresholding has the capability to clean the false junctions occurring where two vessels superpose.

While they are applicable onto any 3-D angiographic data, the components of the basic software tool are applied to 3-D cerebrovascular structures in angiographic images. The toolkit achieved tracking a single branch connected to a user-defined point of interest in a user-defined direction, detecting junctions on it, initiating new tracking procedure on sub-branches connected to itself; hence extracting a vascular network connected to a specific point. This way, a vascular network under risk of embolization during an endovascular operation can be determined. The path reaching at a pathology like aneurysm can be highlighted.

Performance evaluation demonstrates that the false junctions due to superposition of branches lead to a dramatic decrease in the performance of the algorithm. Regarding the real patient image data, average sensitivity of the algorithm is calculated as 87%. Note that sensitivity is ideally expected to be 100%, and the difference occurs due to low quality of angiographic images. In the same manner, regarding the real patient image data, average false negative rate of the algorithm is calculated as 12%, while false negative rate is ideally expected to be 0%. The algorithm produces false negatives when superposition of branches occur as if a junction is existing there; eventually the performance of the algorithm is decreased. Phantom experiments demonstrate that if high quality angiography images were used, and methods to discriminate the branches with superposition would be developed and implemented, the algorithm could achieve 100% sensitivity and specificity, 0% false negative rate and 0% false positive rate.

The toolkit can separately visualize branches, network, skeleton, and junctions. Furthermore, clinicians sometimes require to hide the branch; the toolkit is designed in a manner so that connected network can be hidden in the entire image. Volume growing component is an assistant tool for this visualization process, which covers the tracked branches.

This toolkit is not a clinically applicable software tool yet, but the first step to a clinically applicable product is achieved. True network connected to a point is extracted, false network due to superposed branches must be eliminated.

5.2. Future Work

The 3-D vascular connectivity tracking algorithm fails to discriminate two superposed branches, hence, produce false junctions at the superposition locations. At these false junctions, irrelevant branches join to the network. A local thresholding implementation showed that this problem can be overcome. As the first action, a suitable local thresholding algorithm must be implemented on these superposed vessels to block false junction detection and prevent irrelevant branches from joining the network. On the other hand, active contour tracking and surface tracking can be used to detect junctions, while polynomial fitting can be used to detect and distinguish some unnatural paths, such as false junctions due to superposition. Robust optimization and decision making methods can be implemented to increase the performance of the algorithm.

After achieving the elimination of false junction production, application of the algorithm onto arteriovenous malformations is to be considered. The feeders of an AVM are to be determined by the software application. AVMs have different vascular structures than the branches examined so far. Volume interior to an AVM cannot be tracked, while junction detection method cannot produce useful results since there are many junctions in an AVM. A specialized clustering and segmentation method must be developed to determine the branches coming in and going out of AVM.

REFERENCES

[1] World Health Organization. (2004). *Data and statistics*. Available: http://www.who.int/research/en/. Last accessed 18.04.2011.

[2] World Health Organization, (2006). *Mortality Country Fact Sheet.* Available: http://www.who.int/whosis/mort/profiles/mort_euro_tur_turkey.pdf. Last accessed 18.04.2011.

[3] Flasque N., Desvignes M., Constans J. M., and Revenu M., "Acquisition, segmentation and tracking of the cerebral vascular tree on 3D magnetic resonance angiography images," *Medical Image Analysis*, vol. 5, no. 3, pp. 173 - 183, 2001.

[4] Kashyap R. L., Lee T. C., "Building Skeleton Models via 3-D Medial Surface/Axis Thinning Algorithms," *Graphical Models and Image Processing*, vol. 56, pp. 462-478, 1994.

[5] Blumenfeld H., *Neuroanatomy through Clinical Cases*.: Sinauer Associates, Inc., 2002.

[6] Weinrich W., Kretschmann H. J., *Clinical Neuroimaging and Clinical Neuroanatomy*.: Thieme, 2004.

[7] Adams H. P., *Principles of Cerebrovascular Disease*.: Mc Graw Hill Medical, 2006.

[8] National Institutes of Health. (2010). *MedllinePlus*. Available: http://www.nlm.nih.gov/medlineplus/ency/imagepages/18009.htm. Last accessed 18.04.2011.

[9] MD, Lanzieri C.F., MD, Trinidad S.B., MD, Tarr R.W., MD, Sunshine J.L.,

MD, PhD Lewin J.S., MD Pillai J. J.. (2001). *Radiology*. Available: http://radiology.rsna.org/content/218/3/733.figures-only. Last accessed 18.04.2011.

[10] Jefferson University Hospital. (2010). *Cerebral Aneurysm*. Available: http://www.jeffersonhospital.org/diseases-conditions/cerebral-aneurysm.aspx?disease=4581a9cd-6b07-43e0-a729-aa6994d4b750. Last accessed 18.04.2011.

[11] Siemens Medical. (2010). *syngo InSpace 3D.* Available: https://www.medical.siemens.com/webapp/wcs/stores/servlet/PSOptionProductDisplayView?catalogId=-1&catTree=100010,1007660,12751,1013265&langId=-1&productId=16733&storeId=10001. Last accessed 18.04.2011.

[12] UCLA Division of Interventional Radiology. (2010). *Brain Arteriovenous Malformation*. Available: http://www.aneurysm-stroke.com/av-malformation.php. Last accessed 18.04.2011.

[13] Wechsler L., Babikian V., *Imaging Cerebrovascular Disease*.: Butterworth Heinemann, 2003.

[14] Reuze P., Coatrieux J.L., Luo L.M., and Dillenseger J.L., "3-D vessel tracking and quantitation in angio MRI," in *Bioengineering Conference, 1993., Proceedings of the 1993 IEEE Nineteenth Annual Northeast*, mar 1993, pp. 43 -44.

[15] Klose U., Petersen D., and Martos J., "Tracking of cerebral vessels in MR angiography after highpass filtering," *Magnetic Resonance Imaging*, vol. 13, no. 1, pp. 45 - 51, 1995.

[16] Luo S., Lee S., Ma X., Aziz A., and Nowinski W.L., "Automatic extraction of cerebral arteries from magnetic resonance angiography data: Algorithm and validation," *International Congress Series*, vol. 1281, pp. 375 - 380, 2005.

[17] Yeon D., Won J., "Connectivity-based local adaptive thresholding for carotid artery segmentation using MRA images," *Image and Vision Computing*, vol. 23, no. 14, pp. 1277 - 1287, 2005.

[18] Collorec R., Coatrieux J. L., "Vectorial tracking and directed contour finder for vascular network in digital subtraction angiography," *Pattern Recognition Letters*, vol. 8, no. 5, pp. 353 - 358, 1988.

[19] Kutka R., Stier S., "Extraction of line properties based on direction fields," *Medical Imaging, IEEE Transactions on*, vol. 15, no. 1, pp. 51 -58, feb 1996.

[20] Quek f. K. H., Kirbas C., "Vessel extraction in medical images by wave-propagation and traceback," *Medical Imaging, IEEE Transactions on*, vol. 20, no. 2, pp. 117 -131, feb 2001.

[21] Felkel P., Wegenkittl R., Kanitsar A., "Vessel tracking in peripheral CTA datasets-an overview," in *Computer Graphics, Spring Conference on, 2001.*, 2001, pp. 232 -239.

[22] Kirbas C., Quek F. K. H., "Vessel extraction techniques and algorithms: a survey," in *Bioinformatics and Bioengineering, 2003. Proceedings. Third IEEE Symposium on*, march 2003, pp. 238 - 245.

[23] Luo S., Zhong Y., "Extraction of Brain Vessels from Magnetic Resonance Angiographic Images: Concise Literature Review, Challenges, and Proposals," in *Engineering in Medicine and Biology Society, 2005. IEEE-EMBS 2005. 27th Annual International Conference of the*, 2005, pp. 1422 -1425.

[24] Liu I., Sun Y., "Recursive tracking of vascular networks in angiograms based on the detection-deletion scheme," *Medical Imaging, IEEE Transactions on*, vol. 12, no. 2, pp. 334 -341, jun 1993.

[25] Hadjiiski L. M., Zhou C., Wei J., "Computerized detection of pulmonary embolism in 3D computed tomographic (CT) images: vessel tracking and

segmentation techniques," *Proc. SPIE 5032,* vol. 1613, pp. doi:10.1117/12.481369, 2003.

[26] Bullitt E., Aylward S., Liu A., Stone J., Mukherji S. K., Coffey C., Gerig G., Pizer S. M., "3D graph description of the intracerebral vasculature from segmented MRA and tests of accuracy by comparison with x-ray angiograms", *Information Processing in Medical Imaging*, Springer Berlin / Heidelberg, vol. 1613, pp. 308-321, 1999.

[27] Carrillo J., Hoyos M., Davila E., Orkisz M., "Recursive tracking of vascular tree axes in 3D medical images," *International Journal of Computer Assisted Radiology and Surgery*, vol. 1, pp. 331-339, 2007.

[28] Palagyi K., "A 3D fully parallel surface-thinning algorithm," *Theoretical Computer Science*, vol. 406, no. 1-2, pp. 119 - 135, 2008.

[29] Reinders F., Melvin E. D., and Post F. H., "Skeleton Graph Generation for Feature Shape Description," in *In Joint Eurographics, IEEE TCVG Symposium on Visualization*, 2000, pp. 73--82.

[30] Palagyi K., Kuba A., "A 3D 6-subiteration thinning algorithm for extracting medial lines," *Pattern Recognition Letters*, vol. 19, no. 7, pp. 613 - 627, 1998.

[31] Klette G., Pan M., "A revision of a 3D skeletonization algorithm," University of Auckland, Centre of Image Technology and Robotics, Auckland,.

[32] Palagyi K., Nemeth G., "Fully parallel 3D thinning algorithms based on sufficient conditions for topology preservation," in *Proceedings of the 15th IAPR international conference on Discrete geometry for computer imagery*, Berlin, Heidelberg, 2009, pp. 481--492.

[33] Pitas I,. Nikolaidis N., *3-D image processing algorithms*. New York: John Wiley, 2001.

[34] Leite N. J., Bezerra F. N., "Some comments on thinning algorithms for 3-

D images," Relatorio Tecnico, 1998.

[35] Woods R. E., Gonzalez R. C., *Digital Image Processing*.: Prentice Hall, 2002.

[36] Palagyi K., Tschirren J., Sonka M., "Quantitative analysis of intrathoracic airway trees: Methods and validation", *Information Processing in Medical Imaging*, Springer Berlin / Heidelberg, 2003, vol. 2732, pp. 222-233.

[37] Palagyi K., Balogh E., Kuba A., Halmai C., Erdohelyi B., Sorantin E., Hausegger K., "A sequential 3D thinning algorithm and its medical applications", *Information Processing in Medical Imaging,* Springer Berlin / Heidelberg, 2001, vol. 2082, pp. 409-415.

[38] Chutatape O., Zheng L., Krishnan S.M., "Retinal blood vessel detection and tracking by matched Gaussian and Kalman filters," in *Engineering in Medicine and Biology Society,* 1998. *Proceedings of the 20th Annual International Conference of the IEEE*, vol. 6, oct-1 # nov 1998, pp. 3144 - 3149 vol.6.

[39] Tao Y., Gao Q., "Vessel Junction Detection From Retinal Images," in *16th International Conference on Vision Interface*, Citeseer.

[40] Quelhas P., Boyce J., "Vessel segmentation and branching detection using an adaptive profile Kalman filter in retinal blood vessel structure analysis", *Pattern Recognition and Image Analysis,* Springer Berlin / Heidelberg, 2003, vol. 2652, pp. 802-809.

[41] Leandro J. J. G., Cesar R. M., Costa L. F., "Determining the branchings of 3D structures from respective 2D projections," in *Computer Graphics and Image Processing, 2006. SIBGRAPI '06. 19th Brazilian Symposium on*, oct. 2006, pp. 331 -340.

[42] Zhou J., Chang S., Metaxas D., Axel L., "Vascular structure segmentation and bifurcation detection," in *Biomedical Imaging: From Nano to Macro, 2007. ISBI 2007. 4th IEEE International Symposium on*, april 2007, pp.

872 -875.

[43] Friman O., Hindennach M., Kuhnel C., Peitgen H. O., "Multiple hypothesis template tracking of small 3D vessel structures," *Medical Image Analysis*, vol. 14, no. 2, pp. 160 - 171, 2010.

[44] Fridman Y., Pizer S. M., Aylward S., Bullitt E., "Extracting branching tubular object geometry via cores," *Medical Image Analysis*, vol. 8, no. 3, pp. 169 - 176, 2004.

[45] Laboratory of Neuro Imaging at UCLA. (2008). Available: http://sve.loni.ucla.edu/instructions/metrics/. Last accessed 18.04.2011.

[46] Shattuck D., Prasad G., Mirza M., Narr K. L., Toga A. W., "Online Resource for Validation of Brain Segmentation Methods," *NeuroImage*, vol. 45, pp. 431-439, 2009.